Derivative-based finite-volume MR-HWENO scheme for steady-state problems

Jiayin Li[1], Chi-Wang Shu[2] and Jianxian Qiu[3]

Abstract

In this paper, we further extend the derivative-based finite-volume multi-resolution Hermite weighted essentially non-oscillatory (MR-HWENO) scheme proposed in our previous article (Li, Shu and Qiu, J. Comput. Phys., 446:110653, 2021) to simulate the steady-state problem. When dealing with the steady-state problem, the process of updating and reconstructing the function values is similar to the previous scheme, but the treatment of the derivative values is changed. To be more specific, instead of evolving in time, in the sense of cell averages, the scheme uses the derivative at the current time step and the function at the next time step to reconstruct the derivative at the next time step by direct linear interpolation. There are two advantages for this approach: the first is its high efficiency, when handling the derivative, neither the update on time nor the calculation of nonlinear weights is required; in the meantime, the CFL number can still be taken up to 0.6 as in the original scheme; the second is its strong convergence, the corresponding average residual can quickly converge to machine accuracy, thus obtaining the desired steady-state solution. One- and two-dimensional numerical experiments are given to verify the high efficiency and strong convergence of the proposed MR-HWENO scheme for the steady-state problems.

Key Words: Finite-volume; Multi-resolution scheme; HWENO scheme; Runge-Kutta method; Steady-state problem.

AMS(MOS) subject classification: 65M60, 35L65

[1]School of Mathematical Science, Peking University, Beijing 100871, China; Peking University Chongqing Research Institute of Big Data, Chongqing 400000, China. E-mail: ljy@pku.edu.cn. Research is partly supported by the Postdoctoral Science Foundation of China (Grant No. 2023M740135).

[2]Division of Applied Mathematics, Brown University, Providence, RI 02912, USA. E-mail: Chi-Wang_Shu@brown.edu. Research is partly supported by NSF grant DMS-2309249.

[3]School of Mathematical Sciences and Fujian Provincial Key Laboratory of Mathematical Modeling and High-Performance Scientific Computing, Xiamen University, Xiamen, Fujian 361005, P.R. China. E-mail: jxqiu@xmu.edu.cn. Research is partly supported by NSFC grant 12071392.

1 Introduction

In this paper, we apply the derivative-based finite-volume multi-resolution Hermite weighted essentially non-oscillatory (MR-HWENO) scheme [22] to solve the following steady-state problem:

$$\nabla \cdot \boldsymbol{F}(\boldsymbol{U}) = s(\boldsymbol{U}, \boldsymbol{X}), \tag{1.1}$$

where $\boldsymbol{U}$ is the unknown variable to be determined, $\boldsymbol{F}(\boldsymbol{U})$ is the (usually nonlinear) flux function, $s(\boldsymbol{U}, \boldsymbol{X})$ is the given source term and $\boldsymbol{X} = (x_1, ..., x_d)$. Only one- and two-dimensional cases are considered in this paper, i.e. d=1 or 2, accordingly, we use x to denote x_1, and y to denote x_2.

The steady-state problem is an important mathematical model, which is widely used in a variety of fields such as compressible fluid dynamics, wave motion, advective transport of matter and so on. However, it is not easy to obtain the solution of these problems either theoretically or numerically. One way to solve equation (1.1) numerically is to solve the corresponding unsteady hyperbolic balance law by adopting an appropriate time marching method

$$\begin{cases} \boldsymbol{U}_t + \nabla \cdot \boldsymbol{F}(\boldsymbol{U}) = s(\boldsymbol{U}, \boldsymbol{X}), \\ \boldsymbol{U}(\boldsymbol{X}, 0) = \boldsymbol{U}_0(\boldsymbol{X}). \end{cases} \tag{1.2}$$

With the advance of time, when the residual of the above unsteady hyperbolic balance law (1.2) is sufficiently small, the corresponding solution is considered acceptable as the steady-state solution of (1.1). In this way, we transform the steady-state problem into a time-dependent hyperbolic balance law problem. But in this case, especially for those equations with a nonlinear flux function, discontinuities may appear even if the initial condition is smooth enough. To address this issue, there have existed many works devoted to designing efficient numerical methods to solve these problems with strong shocks or contact discontinuities. A partial list includes essentially non-oscillatory (ENO) schemes in [19, 35, 36], weighted ENO (WENO) schemes in [21, 28] (see also [8]) and Hermite WENO (HWENO) schemes in [30, 31, 40, 43–45].

When solving the steady-state problem using the classical WENO schemes [21, 28] with an appropriate time discretization method [11], we must address the problem that slight post-shock oscillations may propagate downward from the region near the shock to the smooth region, causing the residual to hang at a high truncation error level rather than to stabilize to machine accuracy, see [42]. Although reconstructing the numerical flux using a limiter or an upwind-biased interpolation technique can improve the convergence

of the numerical solution to steady-state as shown in some later papers [33, 41], the residual still fails to converge to machine accuracy for many two-dimensional test cases. For steady-state simulations of Euler equations, Wan and Xia proposed a new hybrid strategy for the fifth-order WENO scheme in [37], which performs better in steady-state convergence property with less dissipative and dispersive errors compared with the existing WENO schemes. They have also extended such scheme to cartesian grids in dealing with the curved geometries in [38]. Another method is to skip the time advance and use the Newton iteration or a more robust method, like the homotopy method [12], which directly solves the nonlinear system derived from a high-order WENO spatial discretization. A possible difficulty of this approach is that such a nonlinear system may have multiple solutions, so we have to screen these solutions carefully to pick out the one we want. Chen proposed a fixed-point fast sweeping WENO method for steady-state solution of scalar hyperbolic conservation laws [6] and since then a series of improved schemes have been put forward, see [24, 25, 39]. Although the convergence of these methods is much improved over the previous schemes, there are still cases where the residual fails to converge to the machine accuracy. Therefore, it is still very urgent to design a numerical scheme that can solve the steady-state problem efficiently.

In order to reduce the computational cost and improve the numerical resolution of the high-resolution scheme near the discontinuities, the multi-resolution method came into being. Initially, Harten proposed the original multi-resolution method for solving the hyperbolic equations in [13–18]. Then Dahmen et al. extended such multi-resolution scheme to solve the conservation laws in [9] and Chiavassa et al. further put forward a multi-resolution-based adaptive scheme to solve the hyperbolic conservation laws in [7]. Later, Abgrall promoted this format to unstructured grids in [1–3]. Shi et al. designed the high-order multi-resolution WENO scheme for complicated flow structures in [34] and Bürger et al. proposed an adaptive multi-resolution WENO scheme for multi-species kinematic flow models in [4]. Recently, Zhu and Shu came up with a new type of multi-resolution WENO (MR-WENO) scheme with increasing higher order of accuracy on the structured and triangular meshes in [46, 48] and then further applied it to solve the steady-state problem in [47]. Based on such finite volume MR-WENO scheme, a new MR-WENO limiter for high-order local discontinuous Galerkin (LDG) method is designed for solving Navier-Stokes equations on triangular meshes in [29]. In general, the main motivation of the multi-resolution method is to concentrate

its computation on those small regions which may contain strong shocks or contact discontinuities.

Inspired by the MR-WENO scheme [46, 48], we have proposed a new type of high-order MR-HWENO scheme to solve the hyperbolic conservation laws on structured meshes in [22] and further improved it in [23]. The main difference between the HWENO scheme and the WENO scheme is that both the function and first-order derivative or moment values are evolved over time and used for reconstruction for HWENO scheme, unlike WENO scheme which only evolves and uses the function values. This also allows the HWENO scheme to obtain the same order of accuracy as the WENO scheme with narrower stencil. When designing this new type of MR-HWENO scheme, we just refer to the original idea of the MR-WENO method, but do not introduce the multi-resolution representation of the solution and data compression. Compared with the classical HWENO schemes, the biggest advantage of such MR-HWENO scheme is that only the function values need to be reconstructed and evolved with HWENO procedure, the first-order derivative or moment values are directly approximated by a high-order linear interpolation. In this paper, we will continue to study the numerical performance of this new type of derivative-based finite-volume MR-HWENO scheme to solve the steady-state problems. The biggest improvement is that the derivatives are not evolved but only linearly reconstructed based on time-misaligned u and v values. It turns out that for both the one- and two-dimensional cases in this paper, the residual of such proposed scheme combined with a third-order total variation diminishing (TVD) Runge-Kutta method can be reduced to machine accuracy or to a tiny value close to machine zero quickly.

The main context of this article is organized as follows. In Section 2, we briefly review the reconstruction process of the derivative-based finite-volume MR-HWENO scheme in [22] and show how to apply it to the steady-state problems in the one- and two-dimensional cases. In Section 3, several classical steady-state testing problems are presented to demonstrate the high efficiency and strong convergence of the proposed scheme. Concluding remarks are given in the last section.

2 Derivative-based finite-volume MR-HWENO scheme

In this section, we will describe the procedure of derivative-based finite-volume MR-HWENO scheme for solving the steady-state problem in one and two dimensions in detail.

2.1 One-dimensional case

To begin with, let us consider the following one-dimensional steady-state problem with a source term on the right side

$$f(u)_x = s(u,x), \quad x \in [x_L, x_R], \tag{2.1}$$

where the source term $s(u,x)$ is related to both the unknown quantity u and the position coordinate x. To solve (2.1), we add the partial derivative of the unknown quantity u with respect to time t to its left side and transform it into the following balance law:

$$u_t + f(u)_x = s(u,x). \tag{2.2}$$

Note that as $t \to \infty$, if the solution of (2.2) tends to the steady-state solution independent of time t, then the solution of (2.1) is obtained. For simplicity, we divide the computational domain by a uniform cell mesh $\{x_{i+1/2}\}_{i=0}^{N}$, where N is the number of cells and $x_{i+1/2}$ is the node. Then, we denote the mesh size by $\triangle x = x_{i+1/2} - x_{i-1/2} = (x_R - x_L)/N$, the cell by $I_i = [x_{i-1/2}, x_{i+1/2}]$ and its center by $x_i = \frac{1}{2}(x_{i-1/2} + x_{i+1/2})$.

We integrate (2.2) over the target cell I_i to obtain its integral formulation

$$\frac{d\overline{u}_i(t)}{dt} = -\frac{1}{\triangle x}\left[f\left(u\left(x_{i+1/2},t\right)\right) - f\left(u\left(x_{i-1/2},t\right)\right)\right] + \frac{1}{\triangle x}\int_{I_i} s(u,x)dx, \tag{2.3}$$

where $\overline{u}_i(t)$ is the cell average of u over the target cell I_i, which is defined as

$$\overline{u}_i(t) = \frac{1}{\triangle x}\int_{I_i} u(x,t)dx. \tag{2.4}$$

Then, we approximate (2.3) by the following semi-discrete conservative scheme

$$\frac{d\overline{u}_i(t)}{dt} = -\frac{1}{\triangle x}(\hat{f}_{i+1/2} - \hat{f}_{i-1/2}) + S_i = L(u)_i, \tag{2.5}$$

here the numerical flux $\hat{f}_{i+1/2}$ is chosen to be the Lax-Friedrichs flux, which satisfies the Lipschitz continuity and consistency, and is defined as

$$\hat{f}_{i+1/2} = \hat{f}(u^-_{i+1/2}, u^+_{i+1/2}) = \frac{1}{2}\Big[f\big(u^-_{i+1/2}\big) + f\big(u^+_{i+1/2}\big) - \alpha\big(u^+_{i+1/2} - u^-_{i+1/2}\big)\Big], \tag{2.6}$$

where $u^{\pm}_{i+1/2}$ are the left and right approximations to the point value $u(x_{i+1/2},t)$ by the derivative-based finite-volume MR-HWENO scheme and $\alpha = \max_u |f'(u)|$ is a global quantity. S_i is the approximation of the

integral term in the conservative scheme (2.5) by the four-point Gauss-Lobatto integration

$$\frac{1}{\triangle x}\int_{I_i} s(u,x)dx \approx \sum_{l=1}^{4} \omega_l s\left(u(x_{i+\sigma_l}^{GL},t), x_{i+\sigma_l}^{GL}\right) := S_i, \tag{2.7}$$

where σ_l and w_l represent the corresponding quadrature points and weights defined in the interval $[-\frac{1}{2},\frac{1}{2}]$

$$\begin{aligned} &\sigma_1 = -\frac{1}{2},\ \sigma_2 = -\frac{\sqrt{5}}{10},\ \sigma_3 = \frac{\sqrt{5}}{10},\ \sigma_4 = \frac{1}{2};\\ &\omega_1 = \omega_4 = \frac{1}{12},\ \omega_2 = \omega_3 = \frac{5}{12}. \end{aligned} \tag{2.8}$$

So here we go, the spatial discretization is complete and our next target is to obtain the values of u at these Gauss-Lobatto points, i.e. $\{u^+_{i-1/2}, u_{i-\sqrt{5}/10}, u_{i+\sqrt{5}/10}, u^-_{i+1/2}\}$ by the derivative-based finite-volume MR-HWENO scheme in [22].

As for the time discretization, we use the third-order TVD Runge-Kutta method

$$\begin{cases} \overline{u}_i^{(1)} = \overline{u}_i^n + \Delta t L(u^n)_i, \\ \overline{u}_i^{(2)} = \frac{3}{4}\overline{u}_i^n + \frac{1}{4}\overline{u}_i^{(1)} + \frac{1}{4}\Delta t L(u^{(1)})_i, \\ \overline{u}_i^{n+1} = \frac{1}{3}\overline{u}_i^n + \frac{2}{3}\overline{u}_i^{(2)} + \frac{2}{3}\Delta t L(u^{(2)})_i, \end{cases} \tag{2.9}$$

where n corresponds to time step $t^n = t^{n-1} + \triangle t$ and the nonconstant time step satisfies

$$\triangle t \max_{1\le i\le N}\left(\frac{|f'(\overline{u}_i)|}{\triangle x}\right) = CFL = 0.6. \tag{2.10}$$

At this point, we have finished the description of the complete algorithm process. The specific reconstruction and evolution procedure is as follows:

One-dimensional Reconstruction and Evolution Algorithm:

Step 1. Reconstruct the Gauss-Lobatto point values of u i.e.$\{(u^n_{i-1/2})^+, u^n_{i-\sqrt{5}/10}, u^n_{i+\sqrt{5}/10}, (u^n_{i+1/2})^-\}$ at the current time step t^n using the given cell averages $\{\overline{u}_l^n, \overline{v}_l^n | l = i-1, i, i+1\}$ by the MR-HWENO scheme in [22]. Here, like the definition of $\overline{u}_i$ in (2.4), $\overline{v}_i$ represents the cell average of $v = u_x$ over the target cell I_i, which can be expressed as

$$\overline{v}_i(t) = \frac{1}{\triangle x}\int_{I_i} v(x,t)dx = \frac{1}{\triangle x}\int_{I_i} u_x(x,t)dx. \tag{2.11}$$

Step 1.1. Select a series of central spatial stencils and reconstruct four polynomials with different

degrees, which meet the following conditions respectively

$$\begin{aligned}
&\frac{1}{\triangle x}\int_{I_k} q_1(x)dx=\overline{u}_k^n, \quad k=i;\\
&\frac{1}{\triangle x}\int_{I_k} q_2(x)dx=\overline{u}_k^n, \quad k=i-1,i,i+1;\\
&\frac{1}{\triangle x}\int_{I_k} q_3(x)dx=\overline{u}_k^n, \quad k=i-1,i,i+1; \quad \frac{1}{\triangle x}\int_{I_{k_x}} q_3'(x)dx=\overline{v}_{k_x}^n, \quad k_x=i;\\
&\frac{1}{\triangle x}\int_{I_k} q_4(x)dx=\overline{u}_k^n, \quad k=i-1,i,i+1; \quad \frac{1}{\triangle x}\int_{I_{k_x}} q_4'(x)dx=\overline{v}_{k_x}^n, \quad k_x=i-1,i,i+1.
\end{aligned} \tag{2.12}$$

Here, $q_1(x)$ is a zeroth degree polynomial, $q_2(x)$ is a quadratic polynomial, $q_3(x)$ is a cubic polynomial and $q_4(x)$ is a quintic polynomial. Then, we rewrite these polynomials as

$$p_{l_2}(x)=\begin{cases} q_1(x), & l_2=1,\\ \dfrac{1}{\gamma_{l_2,l_2}}q_{l_2}(x)-\displaystyle\sum_{l=1}^{l_2-1}\frac{\gamma_{l,l_2}}{\gamma_{l_2,l_2}}p_l(x), & l_2=2,3,4, \end{cases} \tag{2.13}$$

with $\sum_{l=1}^{l_2}\gamma_{l,l_2}=1, \gamma_{l_2,l_2}\neq 0, l_2=2,3,4$, where these γ_{l_1,l_2} for $l_1=1,...,l_2; l_2=2,3,4$ are the linear weights and are defined as

$$\gamma_{l_1,l_2}=\frac{\overline{\gamma}_{l_1,l_2}}{\displaystyle\sum_{l=1}^{l_2}\overline{\gamma}_{l,l_2}}; \quad \overline{\gamma}_{l_1,l_2}=10^{l_1-1}; \quad l_1=1,...,l_2;\ l_2=2,3,4. \tag{2.14}$$

Step 1.2. Compute the smoothness indicator β_{l_2} of polynomial $p_{l_2}(x)$ in the interval I_i:

$$\beta_{l_2}=\sum_{\alpha=1}^{\kappa}\int_{I_i}\triangle x^{2\alpha-1}\left(\frac{d^\alpha p_{l_2}(x)}{dx^\alpha}\right)^2 dx, \quad l_2=2,3,4, \tag{2.15}$$

where $\kappa=2,3,5$ for $l_2=2,3,4$. As for the special case β_1, we refer to the specific algorithm in article [22] and skip the details here. After all these $\beta_{l_2}, l_2=1,2,3,4$ are obtained, we adopt the logic of WENO-Z to define the corresponding nonlinear weights

$$\omega_{l_1,4}=\frac{\overline{\omega}_{l_1,4}}{\displaystyle\sum_{l=1}^{4}\overline{\omega}_{l,4}}, \quad \overline{\omega}_{l_1,4}=\gamma_{l_1,4}\left(1+\left(\frac{\tau_4}{\beta_{l_1}+\varepsilon}\right)^p\right), \quad l_1=1,...,4, \tag{2.16}$$

where $p=2$, ε is taken to be 10^{-6} and the quantity τ_4 is used to measure the average difference between β_4 and the other three smoothness indicators $\beta_{l_2}, l_2=1,2,3$, whose expression is

$$\tau_4=\left(\frac{\displaystyle\sum_{l=1}^{3}|\beta_4-\beta_l|}{3}\right)^2. \tag{2.17}$$

Step 1.3. Obtain a convex combination of the above polynomials $p_{l_2}(x)$ as follows:

$$u_i^n(x)=\sum_{l=1}^{4}\omega_{l,4}p_l(x), \tag{2.18}$$

to approximate u at the current time step t^n and its corresponding Gauss-Lobatto point values are

$$(u^n_{i-1/2})^+ = u^n_i(x_{i-1/2}),\ u^n_{i\mp\sqrt{5}/10} = u^n_i(x_{i\mp\sqrt{5}/10}),\ (u^n_{i+1/2})^- = u^n_i(x_{i+1/2}). \tag{2.19}$$

It is worth noting that we no longer require the reconstructed polynomial of v, which differs from [22].

Step 2. Substitute the values obtained in the previous step into the first stage of the Runge-Kutta formula (2.9), then the cell average $\overline{u}^{(1)}_i$ at the next time stage $t^{(1)}$ can be obtained.

Step 3. Calculate the cell average $\overline{v}^{(1)}_i$ at the next time stage $t^{(1)}$ using the given cell averages $\{\overline{u}^{(1)}_{i-1}, \overline{u}^{(1)}_i, \overline{u}^{(1)}_{i+1}; \overline{v}^n_{i-1}, \overline{v}^n_{i+1}\}$ by a direct linear interpolation. That is, we reconstruct a quartic polynomial, which satisfies

$$\frac{1}{\triangle x}\int_{I_k} p_0(x)dx = \overline{u}^{(1)}_k, \quad k = i-1, i, i+1; \quad \frac{1}{\triangle x}\int_{I_{k_x}} p_0'(x)dx = \overline{v}^n_{k_x}, \quad k_x = i-1, i+1, \tag{2.20}$$

and then, the cell average $\overline{v}^{(1)}_i$ at the next time stage $t^{(1)}$ can be expressed as

$$\overline{v}^{(1)}_i = \frac{1}{\triangle x}\int_{I_i} p_0'(x)dx = \frac{1}{\triangle x}\left(-\frac{3}{4}\overline{u}^{(1)}_{i-1} + \frac{3}{4}\overline{u}^{(1)}_{i+1}\right) - \frac{1}{4}\overline{v}^n_{i-1} - \frac{1}{4}\overline{v}^n_{i+1}. \tag{2.21}$$

Step 4. In ***Step 1***, replace $\overline{u}^n_i$ with $\overline{u}^{(1)}_i$, $\overline{v}^n_i$ with $\overline{v}^{(1)}_i$, and then repeat it to obtain $\{(u^{(1)}_{i-1/2})^+, u^{(1)}_{i-\sqrt{5}/10}$, $u^{(1)}_{i+\sqrt{5}/10}$, $(u^{(1)}_{i+1/2})^-\}$. Then, in ***Step 2***, plug these values into the second stage of the Runge-Kutta formula (2.9) to obtain the cell average $\overline{u}^{(2)}_i$ at the next time stage $t^{(2)}$. Finally, in ***Step 3***, replace $\overline{u}^{(1)}_i$ with $\overline{u}^{(2)}_i$, $\overline{v}^n_i$ with $\overline{v}^{(1)}_i$, and then repeat it to obtain $\overline{v}^{(2)}_i$.

Step 5. In ***Step 1***, replace $\overline{u}^n_i$ with $\overline{u}^{(2)}_i$, $\overline{v}^n_i$ with $\overline{v}^{(2)}_i$, and then repeat it to obtain $\{(u^{(2)}_{i-1/2})^+, u^{(2)}_{i-\sqrt{5}/10}$, $u^{(2)}_{i+\sqrt{5}/10}$, $(u^{(2)}_{i+1/2})^-\}$. Then, in ***Step 2***, plug these values into the third stage of the Runge-Kutta formula (2.9) to obtain the cell average $\overline{u}^{n+1}_i$ at the next time step t^{n+1}. Finally, in ***Step 3***, replace $\overline{u}^{(1)}_i$ with $\overline{u}^{n+1}_i$, $\overline{v}^n_i$ with $\overline{v}^{(2)}_i$, and then repeat it to obtain $\overline{v}^{n+1}_i$.

Step 6. Define the average residual as

$$\frac{\sum_{i=1}^{N}\sum_{k=1}^{m}|(R_k)_i|}{mN}, \tag{2.22}$$

where $(R_k)_i = \frac{\partial(u_k)}{\partial t}|_i \approx \frac{(\overline{u}_k)^{n+1}_i - (\overline{u}_k)^n_i}{\triangle t}$ is the local residual of the k-th component of the variable u in cell I_i, m is the number of components of the variable u and N is the total number of grid cells. Repeat the whole algorithm until the average residual is smaller than the given tolerance value $\epsilon = 10^{-13}$ (this is also the

so-called machine accuracy) or the step number reaches 4000 (except for 200000 for the nozzle flow problem in Example 3.4).

Remark. The updating strategy shown in Formula (2.21) can not be directly extended to the unsteady problems, since there is a misalignment in time when updating the derivative, which leads to a drop in order. To be specific, in terms of the time accuracy at time stage t^n, the cell average $\overline{v}_i^n$ drops to first order (through Taylor expansion in Formula (2.23)) and accordingly the cell average $\overline{u}_i^n$ is reduced to the second order.

$$\begin{aligned}
&\overline{v}_i^n - \frac{1}{\triangle x}\int_{I_i} v(x,t_n)dx \\
&= \left[\frac{1}{\triangle x}\left(-\frac{3}{4}\overline{u}_{i-1}^n + \frac{3}{4}\overline{u}_{i+1}^n\right) - \frac{1}{4}\overline{v}_{i-1}^{n-1} - \frac{1}{4}\overline{v}_{i+1}^{n-1}\right] - \frac{1}{\triangle x}\int_{I_i} v(x,t_n)dx \\
&= \left[-u_{xt}(x_i,t_n) - \frac{3}{2}u_{xx}(x_i,t_n)\right]\triangle t + \left[\frac{9}{16}u_{xxx}(x_i,t_n) - \frac{1}{2}u_{xtt}(x_i,t_n)\right]\triangle t^2.
\end{aligned} \tag{2.23}$$

2.2 Two-dimensional case

Let us now move on to the two-dimensional case

$$f(u)_x + g(u)_y = s(u,x,y), \quad (x,y) \in [x_L, x_R] \times [y_D, y_U], \tag{2.24}$$

where there is a source term $s(u,x,y)$ on the right side of equation (2.24), which depends on both the unknown quantity u and the position coordinate (x,y). Similar to the operation in one dimension, we add the partial derivative of the unknown quantity u with respect to time t to the left side of equation (2.24) and rewrite it as the following balance law:

$$u_t + f(u)_x + g(u)_y = s(u,x,y). \tag{2.25}$$

Likewise, the solution of (2.25) approaches to the steady-state solution independent of time t, that is, the solution of (2.24) when $t \to \infty$. For the sake of simplicity, we consider a uniform cell mesh $\{(x_{i+1/2}, y_{j+1/2})\}_{i=0,j=0}^{N_x,N_y}$, where N_x and N_y are the numbers of cells in the x and y directions, respectively, and $(x_{i+1/2}, y_{j+1/2})$ is the node. Next, we define the mesh size as $\triangle x = x_{i+1/2} - x_{i-1/2} = \frac{x_R - x_L}{N_x}$ in the x-direction and $\triangle y = y_{j+1/2} - y_{j-1/2} = \frac{y_U - y_D}{N_y}$ in the y-direction, the cell as $I_{i,j} = [x_{i-1/2}, x_{i+1/2}] \times [y_{j-1/2}, y_{j+1/2}]$ and its center as $(x_i, y_j) = \left(\frac{1}{2}\left(x_{i-1/2} + x_{i+1/2}\right), \frac{1}{2}\left(y_{j-1/2} + y_{j+1/2}\right)\right)$.

We integrate (2.25) over the target cell $I_{i,j}$ to obtain the corresponding integral formulation

$$\begin{aligned}\frac{d\tilde{\bar{u}}_{i,j}(t)}{dt} =& -\frac{1}{\triangle x\triangle y}\int_{y_{j-1/2}}^{y_{j+1/2}}\left[f\left(u(x_{i+1/2},y,t)\right)-f\left(u(x_{i-1/2},y,t)\right)\right]dy\\ &-\frac{1}{\triangle x\triangle y}\int_{x_{i-1/2}}^{x_{i+1/2}}\left[g\left(u(x,y_{j+1/2},t)\right)-g\left(u(x,y_{j-1/2},t)\right)\right]dx\\ &+\frac{1}{\triangle x\triangle y}\iint_{I_{i,j}} s(u,x,y)dxdy,\end{aligned} \tag{2.26}$$

where $\tilde{\bar{u}}_{i,j}(t)$ is the cell average of u on the target cell $I_{i,j}$, which can be expressed as

$$\tilde{\bar{u}}_{i,j}(t)=\frac{1}{\triangle x\triangle y}\iint_{I_{i,j}} u(x,y,t)dxdy. \tag{2.27}$$

Next, we approximate (2.26) by the following semi-discrete conservative scheme

$$\frac{d\tilde{\bar{u}}_{i,j}(t)}{dt}=-\frac{1}{\triangle x}\left(\hat{F}_{i+\frac{1}{2},j}-\hat{F}_{i-\frac{1}{2},j}\right)-\frac{1}{\triangle y}\left(\hat{G}_{i,j+\frac{1}{2}}-\hat{G}_{i,j-\frac{1}{2}}\right)+S_{i,j}=L(u)_{i,j}, \tag{2.28}$$

again the Lax-Friedrichs flux is used to define the numerical flux and the integral terms in the scheme (2.28) are approximated by a four-point Gauss-Lobatto integration, for instance

$$\begin{aligned}&\frac{1}{\triangle x\triangle y}\iint_{I_{i,j}} s(u,x,y)dxdy\approx\sum_{k=1}^{4}\sum_{l=1}^{4}\omega_k\omega_l s\left(u\left(x_{i+\sigma_k}^{GL},y_{i+\sigma_l}^{GL}\right),x_{i+\sigma_k}^{GL},y_{i+\sigma_l}^{GL}\right):=S_{i,j},\\ &\frac{1}{\triangle y}\int_{y_{j-1/2}}^{y_{j+1/2}}\hat{f}\left(u(x_{i+1/2},y,t)\right)dy\approx\sum_{l=1}^{4}\omega_l\hat{f}\left(u(x_{i+1/2},y_{j+\sigma_l}^{GL},t)\right):=\hat{F}_{i+1/2,j},\\ &\frac{1}{\triangle x}\int_{x_{i-1/2}}^{x_{i+1/2}}\hat{g}\left(u(x,y_{j+1/2},t)\right)dx\approx\sum_{k=1}^{4}\omega_k\hat{g}\left(u(x_{i+\sigma_k}^{GL},y_{j+1/2},t)\right):=\hat{G}_{i,j+1/2},\end{aligned} \tag{2.29}$$

where the definitions of the weights ω_l and the quadrature points σ_l are the same as those in the formula (2.8). Up to now, we have finished the description of the spatial discretization and our next objective is to reconstruct the values of these Gauss-Lobatto points i.e. $\{u^{\pm}_{i\mp1/2,j+\sigma_l},u^{\pm}_{i+\sigma_k,j\mp1/2}|k,l=1,2,3,4;u_{i+\sigma_k,j+\sigma_l}|k,l=2,3\}$ by the derivative-based finite-volume MR-HWENO scheme in [22].

To discretize time, we still use the third-order TVD Runge-Kutta method

$$\begin{cases}\tilde{\bar{u}}^{(1)}_{i,j}=\tilde{\bar{u}}^{n}_{i,j}+\Delta tL(u^n)_{i,j},\\ \tilde{\bar{u}}^{(2)}_{i,j}=\frac{3}{4}\tilde{\bar{u}}^{n}_{i,j}+\frac{1}{4}\tilde{\bar{u}}^{(1)}_{i,j}+\frac{1}{4}\Delta tL(u^{(1)})_{i,j},\\ \tilde{\bar{u}}^{n+1}_{i,j}=\frac{1}{3}\tilde{\bar{u}}^{n}_{i,j}+\frac{2}{3}\tilde{\bar{u}}^{(2)}_{i,j}+\frac{2}{3}\Delta tL(u^{(2)})_{i,j},\end{cases} \tag{2.30}$$

where n also corresponds to the time step $t^n=t^{n-1}+\triangle t$ and the nonconstant time step satisfies

$$\triangle t\max_{1\le i\le N_x,1\le j\le N_y}\left(\frac{|f'(\tilde{\bar{u}}_{i,j})|}{\triangle x}+\frac{|g'(\tilde{\bar{u}}_{i,j})|}{\triangle y}\right)=CFL=0.6. \tag{2.31}$$

At this point, we have obtained the complete discrete scheme and the detailed process is displayed as follows:

Two-dimensional Reconstruction and Evolution Algorithm:

7	8	9	$j+1$
4	5	6	j
1	2	3	$j-1$
$i-1$	i	$i+1$	

The big stencil and its new labels.

Step 1. Reconstruct the Gauss-Lobatto point values of u i.e. $\{(u^n_{i\mp1/2,j+\sigma_l})^{\pm},(u^n_{i+\sigma_k,j\mp1/2})^{\pm}|k,l=1,2,3,4;\ u^n_{i+\sigma_k,j+\sigma_l}|k,l=2,3\}$ at the current time step t^n using the given cell averages $\{\tilde{\bar{u}}^n_{k,l},\tilde{\bar{v}}^n_{k,l},\tilde{\bar{w}}^n_{k,l}|k=i-1,i,i+1;l=j-1,j,j+1\}$ by the derivative-based finite-volume MR-HWENO scheme in [22]. Again, like the definition of $\tilde{\bar{u}}_{i,j}$ in (2.27), $\tilde{\bar{v}}_{i,j}$ and $\tilde{\bar{w}}_{i,j}$ indicate the cell averages of $v=u_x$ and $w=u_y$ over the target cell $I_{i,j}$ respectively, which can be taken as

$$\begin{cases}\tilde{\bar{v}}_{i,j}(t)=\dfrac{1}{\triangle x\triangle y}\displaystyle\iint_{I_{i,j}}v(x,y,t)dxdy=\dfrac{1}{\triangle x\triangle y}\iint_{I_{i,j}}u_x(x,y,t)dxdy,\\ \tilde{\bar{w}}_{i,j}(t)=\dfrac{1}{\triangle x\triangle y}\displaystyle\iint_{I_{i,j}}w(x,y,t)dxdy=\dfrac{1}{\triangle x\triangle y}\iint_{I_{i,j}}u_y(x,y,t)dxdy.\end{cases}\tag{2.32}$$

Step 1.1. Select a series of nested central templates and reconstruct four polynomials of different degrees, which satisfy the following conditions respectively

$$\begin{aligned}
&\text{For } q_1(x,y):\frac{1}{\triangle x\triangle y}\iint_{I_k}q_1(x,y)dxdy=\tilde{\bar{u}}^n_k,\quad k=5.\\
&\text{For } q_2(x,y):\frac{1}{\triangle x\triangle y}\iint_{I_k}q_2(x,y)dxdy=\tilde{\bar{u}}^n_k,\quad k=1,...,9.\\
&\text{For } q_3(x,y):\frac{1}{\triangle x\triangle y}\iint_{I_k}q_3(x,y)dxdy=\tilde{\bar{u}}^n_k,\quad k=1,...,9;\\
&\qquad\frac{1}{\triangle x\triangle y}\iint_{I_{k_x}}\frac{\partial q_3(x,y)}{\partial x}dxdy=\tilde{\bar{v}}^n_{k_x},\quad k_x=5;\\
&\qquad\frac{1}{\triangle x\triangle y}\iint_{I_{k_y}}\frac{\partial q_3(x,y)}{\partial y}dxdy=\tilde{\bar{w}}^n_{k_y},\quad k_y=5.\\
&\text{For } q_4(x,y):\frac{1}{\triangle x\triangle y}\iint_{I_k}q_4(x,y)dxdy=\tilde{\bar{u}}^n_k,\quad k=1,...,9;\\
&\qquad\frac{1}{\triangle x\triangle y}\iint_{I_{k_x}}\frac{\partial q_4(x,y)}{\partial x}dxdy=\tilde{\bar{v}}^n_{k_x},\quad k_x=1,3,4,5,6,7,9;\\
&\qquad\frac{1}{\triangle x\triangle y}\iint_{I_{k_y}}\frac{\partial q_4(x,y)}{\partial y}dxdy=\tilde{\bar{w}}^n_{k_y},\quad k_y=1,2,3,5,7,8,9.
\end{aligned}\tag{2.33}$$

Compared to the one-dimensional case, the similarity is that the degrees of $q_1(x,y)$, $q_2(x,y)$, $q_3(x,y)$ and $q_4(x,y)$ are the same as those of $q_1(x)$, $q_2(x)$, $q_3(x)$ and $q_4(x)$ in (2.12) respectively, but the difference is

that except for $q_1(x,y)$, the other three polynomials do not satisfy all the required equalities exactly. This is because the number of unknowns in finding the coefficients of these polynomials is smaller than the number of equations. Thus we require these three polynomials to have the same cell average as u on the target cell $I_{i,j}$ (to ensure conservation) and in the meantime we match the other conditions in the sense of least squares as described in [20]. Next, we rewrite the polynomials above as

$$p_{l_2}(x,y)=\begin{cases} q_1(x,y), & l_2=1,\\ \dfrac{1}{\gamma_{l_2,l_2}}q_{l_2}(x,y)-\displaystyle\sum_{l=1}^{l_2-1}\frac{\gamma_{l,l_2}}{\gamma_{l_2,l_2}}p_l(x,y), & l_2=2,3,4, \end{cases} \tag{2.34}$$

with $\sum_{l=1}^{l_2}\gamma_{l,l_2}=1, \gamma_{l_2,l_2}\neq 0, l_2=2,3,4$, where these γ_{l_1,l_2} for $l_1=1,...,l_2; l_2=2,3,4$ are still the linear weights and are defined the same as (2.14).

Step 1.2. Compute the smoothness indicator β_{l_2} of the polynomial $p_{l_2}(x,y)$ in the target cell $I_{i,j}$:

$$\beta_{l_2}=\sum_{|\alpha|=1}^{\kappa}\iint_{I_{i,j}}|I_{i,j}|^{|\alpha|-1}\left(\frac{\partial^{|\alpha|}}{\partial x^{\alpha_x}\partial y^{\alpha_y}}p_{l_2}(x,y)\right)^2 dxdy, \quad l_2=2,3,4, \tag{2.35}$$

where $\alpha=(\alpha_x,\alpha_y)$, $|\alpha|=\alpha_x+\alpha_y$ and $\kappa=2,3,5$ for $l_2=2,3,4$. For the special choice of β_1, please see the detailed algorithm in [22], and we omit the details here for brevity. Then the idea of WENO-Z is still adopted to define the corresponding nonlinear weights, the specific definition is shown in (2.16).

Step 1.3. Combine the above polynomials $p_{l_2}(x,y)$ to get a new polynomial as follows:

$$u_{i,j}^n(x,y)=\sum_{l=1}^{4}\omega_{l,4}p_l(x,y), \tag{2.36}$$

to approximate u at the current time step t^n and its corresponding Gauss-Lobatto point values are

$$\begin{aligned} (u_{i\mp 1/2,j+\sigma_l}^n)^{\pm}&=u_{i,j}^n(x_{i\mp 1/2},y_{j+\sigma_l}), \quad l=1,2,3,4;\\ (u_{i+\sigma_k,j\mp 1/2}^n)^{\pm}&=u_{i,j}^n(x_{i+\sigma_k},y_{j\mp 1/2}), \quad k=1,2,3,4;\\ u_{i+\sigma_k,j+\sigma_l}^n&=u_{i,j}^n(x_{i+\sigma_k},y_{j+\sigma_l}), \quad k,l=2,3. \end{aligned} \tag{2.37}$$

We note that it is still not necessary to obtain the reconstructed polynomials of v and w as in [22].

Step 2. Plug the values obtained in the previous step into the first stage of the Runge-Kutta formula (2.30) to obtain the cell average $\tilde{\bar{u}}_{i,j}^{(1)}$ at the next time stage $t^{(1)}$.

Step 3. Calculate the cell averages $\tilde{\bar{v}}_{i,j}^{(1)}$ and $\tilde{\bar{w}}_{i,j}^{(1)}$ at the next time stage $t^{(1)}$ using the given cell averages $\{\tilde{\bar{u}}_{i-1,j}^{(1)}, \tilde{\bar{u}}_{i,j}^{(1)}, \tilde{\bar{u}}_{i+1,j}^{(1)}; \tilde{\bar{v}}_{i-1,j}^{n}, \tilde{\bar{v}}_{i+1,j}^{n}\}$ and $\{\tilde{\bar{u}}_{i,j-1}^{(1)}, \tilde{\bar{u}}_{i,j}^{(1)}, \tilde{\bar{u}}_{i,j+1}^{(1)}; \tilde{\bar{w}}_{i,j-1}^{n}, \tilde{\bar{w}}_{i,j+1}^{n}\}$ by a direct linear interpolation,

respectively. That is, reconstruct two quartic polynomials, which satisfy

$$\begin{aligned}
&\frac{1}{\triangle x}\int_{x_{k-1/2}}^{x_{k+1/2}} p_{01}(x)dx = \tilde{\overline{u}}^{(1)}_{k,j}, \quad k = i-1, i, i+1; \quad \frac{1}{\triangle x}\int_{x_{k_x-1/2}}^{x_{k_x+1/2}} p'_{01}(x)dx = \tilde{\overline{v}}^{n}_{k_x,j}, \quad k_x = i-1, i+1;\\
&\frac{1}{\triangle y}\int_{y_{k-1/2}}^{y_{k+1/2}} p_{02}(y)dy = \tilde{\overline{u}}^{(1)}_{i,k}, \quad k = j-1, j, j+1; \quad \frac{1}{\triangle y}\int_{y_{k_y-1/2}}^{y_{k_y+1/2}} p'_{02}(y)dy = \tilde{\overline{w}}^{n}_{i,k_y}, \quad k_y = j-1, j+1,
\end{aligned} \tag{2.38}$$

and next, define the cell averages $\tilde{\overline{v}}^{(1)}_{i,j}$ and $\tilde{\overline{w}}^{(1)}_{i,j}$ at the next time stage $t^{(1)}$ as

$$\begin{aligned}
\tilde{\overline{v}}^{(1)}_{i,j} &= \frac{1}{\triangle x}\int_{x_{i-1/2}}^{x_{i+1/2}} p'_{01}(x)dx = \frac{1}{\triangle x}(-\frac{3}{4}\tilde{\overline{u}}^{(1)}_{i-1,j} + \frac{3}{4}\tilde{\overline{u}}^{(1)}_{i+1,j}) - \frac{1}{4}\tilde{\overline{v}}^{n}_{i-1,j} - \frac{1}{4}\tilde{\overline{v}}^{n}_{i+1,j},\\
\tilde{\overline{w}}^{(1)}_{i,j} &= \frac{1}{\triangle y}\int_{y_{j-1/2}}^{y_{j+1/2}} p'_{02}(y)dy = \frac{1}{\triangle y}(-\frac{3}{4}\tilde{\overline{u}}^{(1)}_{i,j-1} + \frac{3}{4}\tilde{\overline{u}}^{(1)}_{i,j+1}) - \frac{1}{4}\tilde{\overline{w}}^{n}_{i,j-1} - \frac{1}{4}\tilde{\overline{w}}^{n}_{i,j+1}.
\end{aligned} \tag{2.39}$$

Step 4. In ***Step 1***, replace $\tilde{\overline{u}}^{n}_{i,j}$ with $\tilde{\overline{u}}^{(1)}_{i,j}$, $\tilde{\overline{v}}^{n}_{i,j}$ with $\tilde{\overline{v}}^{(1)}_{i,j}$, $\tilde{\overline{w}}^{n}_{i,j}$ with $\tilde{\overline{w}}^{(1)}_{i,j}$ and then repeat it to obtain the Gauss-Lobatto point values $\{(u^{(1)}_{i-1/2,j+\eta_l})^+, (u^{(1)}_{i+1/2,j+\eta_l})^- |\ l = 1,2,3,4;\ (u^{(1)}_{i+\xi_k,j-1/2})^+, (u^{(1)}_{i+\xi_k,j+1/2})^- |\ k = 1,2,3,4;\ u^{(1)}_{i+\xi_k,j+\eta_l} | k,l = 2,3\}$. Then, in ***Step 2***, plug these values into the second stage of the Runge-Kutta formula (2.30) to obtain the cell average $\tilde{\overline{u}}^{(2)}_{i,j}$ at the next time stage $t^{(2)}$. Finally, in ***Step 3***, replace $\tilde{\overline{u}}^{(1)}_{i,j}$ with $\tilde{\overline{u}}^{(2)}_{i,j}$, $\tilde{\overline{v}}^{n}_{i,j}$ with $\tilde{\overline{v}}^{(1)}_{i,j}$, $\tilde{\overline{w}}^{n}_{i,j}$ with $\tilde{\overline{w}}^{(1)}_{i,j}$ and then repeat it to obtain $\tilde{\overline{v}}^{(2)}_{i,j}$ and $\tilde{\overline{w}}^{(2)}_{i,j}$.

Step 5. In ***Step 1***, replace $\tilde{\overline{u}}^{n}_{i,j}$ with $\tilde{\overline{u}}^{(2)}_{i,j}$, $\tilde{\overline{v}}^{n}_{i,j}$ with $\tilde{\overline{v}}^{(2)}_{i,j}$, $\tilde{\overline{w}}^{n}_{i,j}$ with $\tilde{\overline{w}}^{(2)}_{i,j}$ and then repeat it to obtain the Gauss-Lobatto point values $\{(u^{(2)}_{i-1/2,j+\eta_l})^+, (u^{(2)}_{i+1/2,j+\eta_l})^- |\ l = 1,2,3,4;\ (u^{(2)}_{i+\xi_k,j-1/2})^+, (u^{(2)}_{i+\xi_k,j+1/2})^- |\ k = 1,2,3,4;\ u^{(2)}_{i+\xi_k,j+\eta_l} | k,l = 2,3\}$. Then, in ***Step 2***, plug these values into the third stage of the Runge-Kutta formula (2.30) to obtain the cell average $\tilde{\overline{u}}^{n+1}_{i,j}$ at the next time step t^{n+1}. Finally, in ***Step 3***, replace $\tilde{\overline{u}}^{(1)}_{i,j}$ with $\tilde{\overline{u}}^{n+1}_{i,j}$, $\tilde{\overline{v}}^{n}_{i,j}$ with $\tilde{\overline{v}}^{(2)}_{i,j}$, $\tilde{\overline{w}}^{n}_{i,j}$ with $\tilde{\overline{w}}^{(2)}_{i,j}$ and then repeat it to obtain $\tilde{\overline{v}}^{n+1}_{i,j}$ and $\tilde{\overline{w}}^{n+1}_{i,j}$.

Step 6. Repeat the whole reconstruction algorithm until the average residual (2.22) with $N = N_x \times N_y$ is smaller than the given tolerance value $\epsilon = 10^{-13}$ or the step number reaches 4000.

Remark. For one-dimensional systems, the definition of α in (2.6) will become the maximum value of the absolute value of its eigenvalues, i.e. $\alpha = \max_u |\lambda(u)|$, and the CFL condition (2.10) will become

$$\triangle t \max_{1\le k\le m, 1\le i\le N}\left(\frac{|\lambda^k(\overline{u}_i)|}{\triangle x}\right) = CFL = 0.6, \tag{2.40}$$

where λ^k denotes the k-th eigenvalue of the matrix $f'(u)$ and i refers to the i-th cell. Similarly, for two-dimensional systems, the definition of α in (2.6) will become $\alpha = \max_u |\lambda_x(u)|$ in the x-direction and $\alpha = \max_u |\lambda_y(u)|$ in the y-direction, and the CFL condition (2.31) will become

$$\triangle t \max_{1\le k\le m,1\le i\le N_x,1\le j\le N_y}\left(\frac{|\lambda_x^k(\widetilde{u}_{i,j})|}{\triangle x}+\frac{|\lambda_y^k(\widetilde{u}_{i,j})|}{\triangle y}\right)=CFL=0.6, \tag{2.41}$$

where λ_x^k denotes the k-th eigenvalue of the matrix $f'(u)$, λ_y^k denotes the k-th eigenvalue of the matrix $g'(u)$ and i,j refers to the cell in column i, row j.

3 Numerical tests

In this section, we present a number of numerical experiments to test the performance of the proposed derivative-based finite-volume MR-HWENO scheme for scalar and system steady-state problems with source terms in one and two dimensions. Here "MR-HWENO5" represents the fifth-order multi-resolution HWENO scheme, "MR-WENO5" represents the fifth-order multi-resolution WENO scheme and "WENO5-Z" represents the fifth-order WENO-Z scheme. The third-order TVD Runge-Kutta method is used in time for all numerical simulations. The CFL number is taken to be 0.6 for both the one- and two-dimensional cases. Unnormalized linear weights are set to be $\overline{\gamma}_{1,4}=1$, $\overline{\gamma}_{2,4}=10$, $\overline{\gamma}_{3,4}=100$ and $\overline{\gamma}_{4,4}=1000$.

3.1 The one-dimensional problems

Example 3.1. We solve the one-dimensional Burgers' equation:

$$\left(\frac{u^2}{2}\right)_x=\sin x\cos x,\quad x\in[0,\pi], \tag{3.1}$$

with a source term at its right end, which depends only on the position x. The initial condition is

$$u_0(x)=\beta\sin x, \tag{3.2}$$

and the boundary condition is $u(0)=u(\pi)=0$.

This problem has been treated as a typical initial value problem with multiple steady-state solutions in [32], and its steady-state solution depends on the value of β, to be more specific:

(1) If $-1<\beta<1$, there will be a shock wave within the computational domain. This shock wave consists of two branches ($\sin x$ and $-\sin x$) and is located at $x_s=\pi-\arcsin\sqrt{1-\beta^2}$ (derived from the conservation of mass $\int_0^\pi u dx=2\beta$). Under such a circumstance, we take $\beta=0.5$ to test the resolution

of our scheme near the discontinuity. At this point, the shock wave is roughly located at $x_s = 2.0944$. The numerical results of the MR-HWENO5, MR-WENO5 and WENO5-Z schemes versus the exact solution are shown in Figure 3.1. Figure 3.2 shows the convergence history of the average residual varying with the number of iterations. It is observed that the convergence rates of these three schemes are almost the same, but the MR-HWENO5 scheme reaches the steady state with a much smaller residual than the other two schemes.

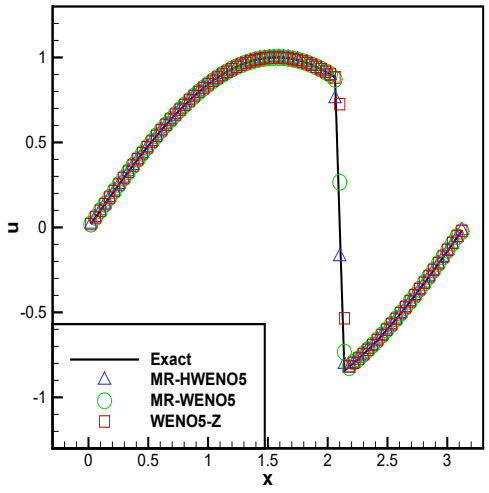

Figure 3.1: 1D-Burgers' equation: $s(x) = \sin x \cos x$, $\beta = 0.5$. The numerical results versus the exact solution. Number of cells: 100.

(2) Otherwise, the solution will be smooth in the open interval, but then forms a shock at the boundary $x = \pi$ (for $\beta \geq 1$) or $x = 0$ (for $\beta \leq -1$), and later converges to a smooth steady state $u(x, \infty) = \sin x$ (for $\beta \geq 1$) or $u(x, \infty) = -\sin x$ (for $\beta \leq -1$), respectively. In this case, we take $\beta = 2$ to test the accuracy of our scheme in the smooth region. The corresponding errors and convergence orders of the MR-HWENO5 (on uniform and non-uniform meshes), MR-WENO5 and WENO5-Z schemes are listed in Table 3.1. Here, the non-uniform mesh is obtained by adding a 20% random disturbance to the uniform mesh, that is, the quasi-uniform mesh. We can see that these four schemes are all of fifth-order in the L^1 norm and fourth-order in the L^∞ norm due to the effect of the shock at the boundary $x = \pi(\beta = 2 \geq 1)$. The error of the MR-HWENO5 scheme on uniform mesh is smaller than that of the MR-HWENO5 scheme on non-uniform mesh and the other two schemes for the same mesh

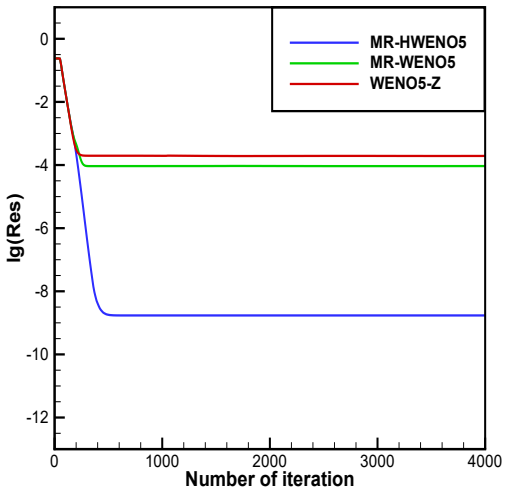

Figure 3.2: 1D-Burgers' equation: $s(x) = \sin x \cos x$, $\beta = 0.5$. The convergence history of the average residual. Number of cells: 100.

size. The convergence history of the average residual varying with the number of iterations is shown in Figure 3.3. It is observed that although the residuals corresponding to all schemes can reach machine accuracy, MR-HWENO5 scheme on uniform mesh declines the fastest.

Table 3.1: 1D-Burgers' equation: $s(x) = \sin x \cos x$, $\beta = 2.0$. The initial condition $u(x, 0) = 2\sin(x)$. The boundary condition $u(0) = u(\pi) = 0$. L^1 and L^∞ error.

	Uniform MR-HWENO5 scheme				Non-uniform MR-HWENO5 scheme			
grid points	L^1 error	order	L^∞ error	order	L^1 error	order	L^∞ error	order
20	4.48E-07		2.33E-06		4.62E-07		2.47E-06	
30	6.99E-08	4.77	5.18E-07	3.87	7.16E-08	4.79	5.29E-07	3.96
40	1.84E-08	4.78	1.70E-07	3.98	1.96E-08	4.63	1.80E-07	3.86
50	6.45E-09	4.79	7.04E-08	4.04	7.56E-09	4.36	8.04E-08	3.69
60	2.73E-09	4.80	3.38E-08	4.09	2.91E-09	5.33	3.64E-08	4.43
70	1.32E-09	4.81	1.81E-08	4.12	1.37E-09	4.96	1.87E-08	4.39
	MR-WENO5 scheme				WENO5-Z scheme			
grid points	L^1 error	order	L^∞ error	order	L^1 error	order	L^∞ error	order
20	3.47E-06		2.38E-05		3.48E-06		2.39E-05	
30	5.16E-07	4.90	3.98E-06	4.59	5.16E-07	4.90	3.98E-06	4.60
40	1.32E-07	4.89	1.26E-06	4.11	1.32E-07	4.89	1.26E-06	4.12
50	4.53E-08	4.89	5.07E-07	4.17	4.53E-08	4.89	5.07E-07	4.17
60	1.89E-08	4.88	2.39E-07	4.21	1.89E-08	4.88	2.39E-07	4.21
70	9.00E-09	4.88	1.26E-07	4.24	9.00E-09	4.88	1.26E-07	4.24

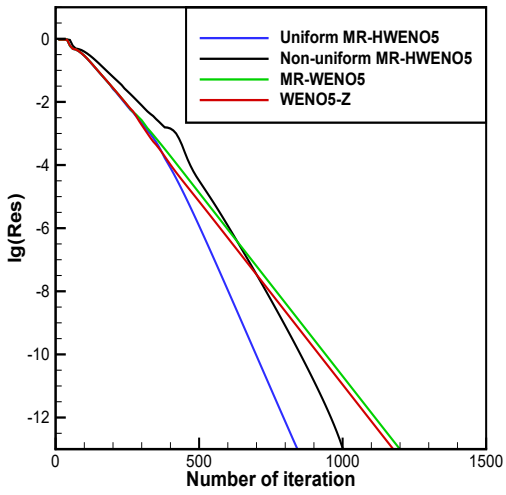

Figure 3.3: 1D-Burgers' equation: $s(x) = \sin x \cos x$, $\beta = 2.0$. The convergence history of the average residual. Number of cells: 70.

Example 3.2. The following is still a one-dimensional Burgers' equation:

$$\left(\frac{u^2}{2}\right)_x = -\pi \cos(\pi x) u, \quad x \in [0, 1], \tag{3.3}$$

but unlike Example 3.1, the source term on the right side hinges on both the position x and the solution u itself. The initial condition is

$$u_0(x) = \begin{cases} 1, & \text{if } 0 \le x < 0.5, \\ -0.1, & \text{if } 0.5 \le x \le 1, \end{cases} \tag{3.4}$$

and the boundary condition is $u(0) = 1$ and $u(1) = -0.1$.

This problem was studied as an example of multiple steady states for one-dimensional transonic flows in [10], which has two steady-state solutions involving a shock

$$u(x) = \begin{cases} u^+ = 1 - \sin(\pi x), & \text{if } 0 \le x < x_s, \\ u^- = -0.1 - \sin(\pi x), & \text{if } x_s \le x \le 1, \end{cases} \tag{3.5}$$

where $x_s = 0.1486$ or $x_s = 0.8514$. Even though both of these solutions satisfy the Rankine-Hugoniot jump condition and the entropy condition, only the first one with a shock at $x_s = 0.1486$ is stable for a small perturbation. For this reason, this problem is always used to demonstrate the good convergence of the scheme. That is to say, although there is a reasonable perturbation in the steady state at the beginning, the numerical solution can still converge to the stable one. Note that the jump in the initial condition lies

between the shock waves of above two admissible steady-state solutions. The numerical results of the MR-HWENO5, MR-WENO5 and WENO5-Z schemes versus the exact solution are shown in Figure 3.4. Figure 3.5 shows the convergence history of the average residual varying with the number of iterations. It is easy to see that the residuals of these three schemes can reduce to machine precision, and the MR-HWENO5 scheme drops slightly faster than the other two schemes.

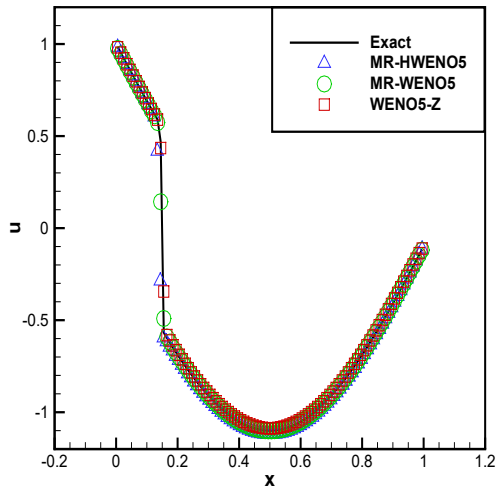

Figure 3.4: 1D-Burgers' equation: $s(u,x) = -\pi\cos(\pi x)u$. The numerical results versus the exact solution. Number of cells: 100.

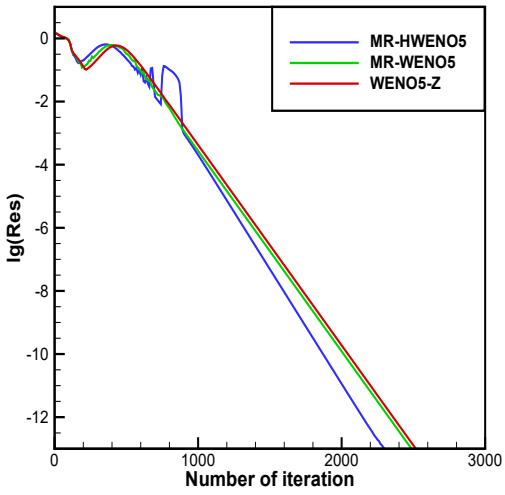

Figure 3.5: 1D-Burgers' equation: $s(u,x) = -\pi\cos(\pi x)u$. The convergence history of the average residual. Number of cells: 100.

Example 3.3. The one-dimensional shallow water equations:

$$\begin{pmatrix} hu \\ hu^2 + \frac{1}{2}gh^2 \end{pmatrix}_x = \begin{pmatrix} 0 \\ -ghb_x \end{pmatrix}, \quad x \in [0, 10], \tag{3.6}$$

where h is the height of the water to the bottom, u is the velocity of the fluid, g is the gravitational constant and function $b(x)$ represents the bottom topography, which is given to be $b(x) = 5\exp^{-\frac{2}{5}(x-5)^2}$. Both the initial condition and the boundary condition are

$$h + b = 10, \quad hu = 0. \tag{3.7}$$

Notice that the initial condition above is stationary, which itself is also a steady-state solution of (3.6). Starting from such a stationary initial condition, we can test out how well our scheme performs in the smooth region. The corresponding errors and convergence orders of the MR-HWENO5, MR-WENO5 and WENO5-Z schemes for h are listed in Table 3.2, where the sixth-order super-convergence rate of these three schemes is observed in L^1 norm and L^∞ norm. Also, the error of the MR-HWENO5 scheme is smaller than that of the other two schemes for the same mesh size. The convergence history of the average residual varying with the number of iterations is shown in Figure 3.6, where there is not much difference between the residuals when the steady state is reached and the rates at which the residuals decrease among these three schemes.

Table 3.2: 1D shallow water equation. The stationary initial condition $h + b = 10, hu = 0$. The exact boundary condition. L^1 and L^∞ error.

	MR-HWENO5 scheme				MR-WENO5 scheme			
grid points	L^1 error	order	L^∞ error	order	L^1 error	order	L^∞ error	order
20	6.34E-05		3.24E-04		2.77E-04		1.87E-03	
30	8.30E-06	6.04	4.45E-05	5.90	3.53E-05	6.13	2.87E-04	5.58
40	1.85E-06	5.97	1.01E-05	5.91	7.49E-06	6.17	6.89E-05	5.68
50	5.55E-07	6.00	3.03E-06	5.98	2.28E-06	5.92	2.12E-05	5.88
60	2.03E-07	6.02	1.12E-06	5.98	8.62E-07	5.83	7.85E-06	5.94
70	8.66E-08	5.95	4.74E-07	5.98	3.74E-07	5.84	3.35E-06	5.96

	WENO5-Z scheme			
grid points	L^1 error	order	L^∞ error	order
20	2.44E-04		7.70E-04	
30	3.86E-05	5.48	1.29E-04	5.31
40	8.72E-06	5.91	3.13E-05	5.64
50	2.62E-06	6.00	9.66E-06	5.86
60	9.72E-07	5.92	3.55E-06	5.99
70	4.16E-07	5.94	1.49E-06	6.05

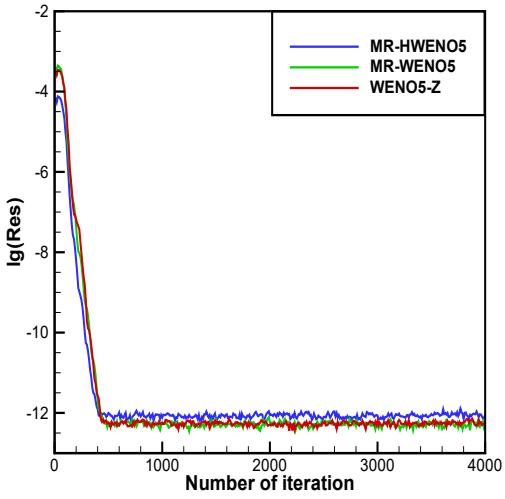

Figure 3.6: 1D shallow water equation. The convergence history of the average residual. Number of cells: 70.

Example 3.4. The one-dimensional nozzle flow problem:

$$\begin{pmatrix} \rho u \\ \rho u^2 + p \\ u(E+p) \end{pmatrix}_x = -\frac{A'(x)}{A(x)} \begin{pmatrix} \rho u \\ \rho u^2 \\ u(E+p) \end{pmatrix}, \quad x \in [0,1], \tag{3.8}$$

where ρ is the density, u is the velocity of the fluid, E is the total energy, $\gamma = 1.4$ is the gas constant, $p = (\gamma - 1)\left(E - \frac{1}{2}\rho u^2\right)$ is the pressure and $A(x)$ represents the area of the cross-section of the nozzle, which is determined by the following relation

$$A(x) f(\text{Mach number at } x) = \text{constant}, \quad \forall x \in [0,1],$$

where

$$f(w) = \frac{w}{(1+\delta_0 w^2)^{p_0}}, \quad \delta_0 = \frac{1}{2}(\gamma - 1), \quad p_0 = \frac{1}{2} \cdot \frac{\gamma+1}{\gamma-1}.$$

The initial condition is an isentropic initial value with a shock at $x = 0.5$. As for the boundary condition, it is taken to be $\rho(x \to -\infty) = p(x \to -\infty) = 1$. The inlet Mach number at $x = 0$ is 0.8, the outlet Mach number at $x = 1$ is 1.8, and the Mach number is linearly distributed before and after the shock wave. The numerical results of the MR-HWENO5 (on uniform and non-uniform meshes), MR-WENO5 and WENO5-Z schemes versus the exact solution are shown in Figure 3.7. Here, the non-uniform mesh is also obtained by adding a 20% random disturbance to the uniform mesh, and the step size of the cells located in the interval [0.4,0.6], where the shock roughly lies, is set to be 1/2 that of the rest of the cells when dividing the initial

uniform grid. Figure 3.8 shows the convergence history of the average residual varying with the number of iterations. It is observed that there is little difference in the residuals corresponding to these four schemes when the steady state is reached, and the MR-HWENO5 scheme on uniform mesh converges faster than the MR-HWENO5 scheme on non-uniform mesh and the other two schemes.

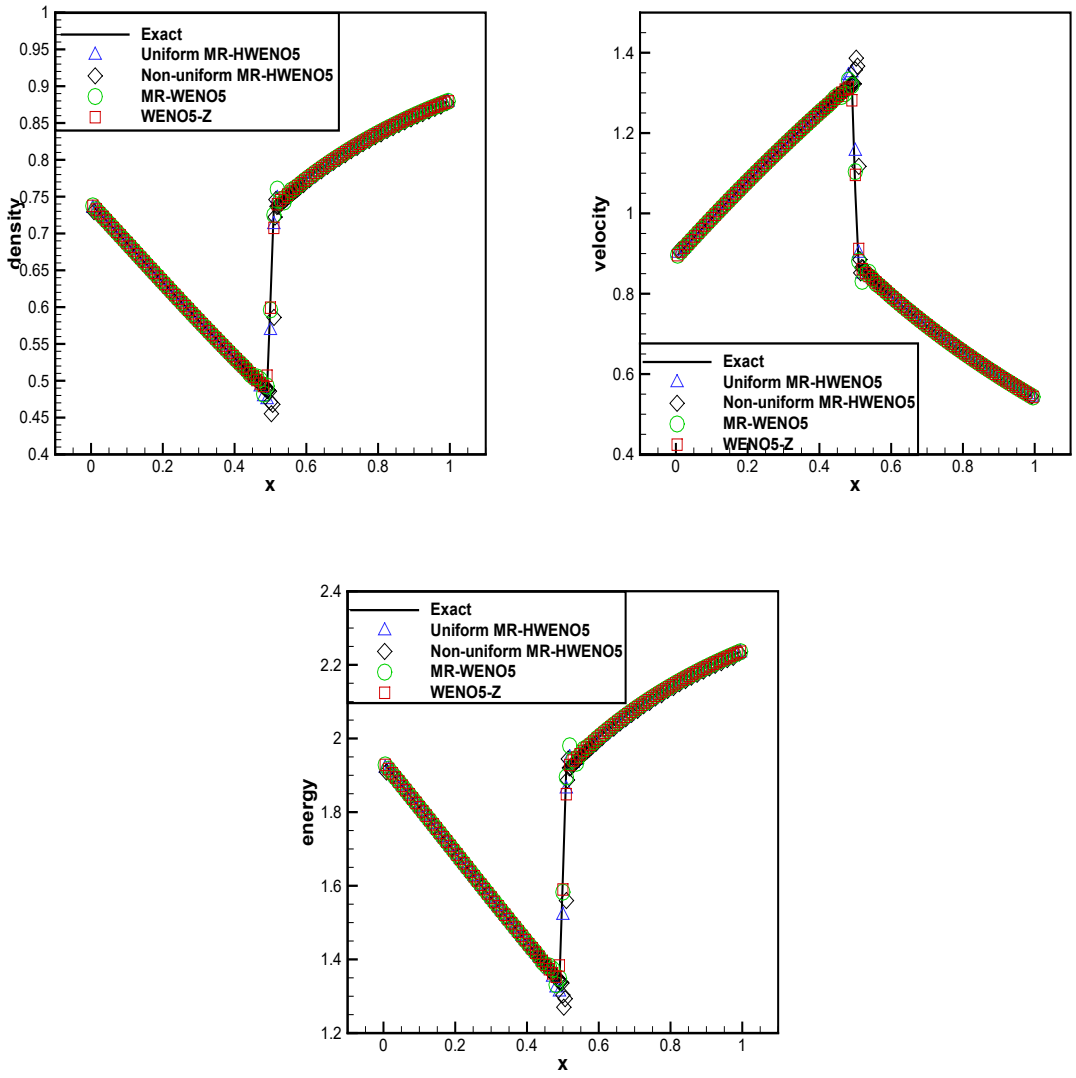

Figure 3.7: 1D nozzle flow problem. The numerical results versus the exact solution. Number of cells: 100.

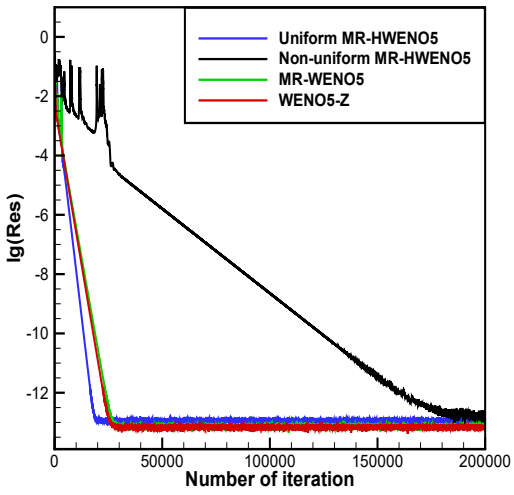

Figure 3.8: 1D nozzle flow problem. The convergence history of the average residual. Number of cells: 100.

3.2 The two-dimensional problems

Example 3.5. The two-dimensional Burgers' equation:

$$\left(\frac{1}{\sqrt{2}}\frac{u^2}{2}\right)_x + \left(\frac{1}{\sqrt{2}}\frac{u^2}{2}\right)_y = \sin\left(\frac{x+y}{\sqrt{2}}\right)\cos\left(\frac{x+y}{\sqrt{2}}\right), \quad (x,y) \in \left[0, \frac{\pi}{\sqrt{2}}\right] \times \left[0, \frac{\pi}{\sqrt{2}}\right], \tag{3.9}$$

where there is a source term that depends only on the position (x, y) at its right end. The initial condition is

$$u_0(x,y) = \beta \sin\left(\frac{x+y}{\sqrt{2}}\right), \tag{3.10}$$

and the boundary condition is taken to be the exact solution of this steady-state problem.

In terms of the equation form, this problem seems to be a special case of the one-dimensional **Example 3.1** along the northeast-southwest diagonal, but essentially it is a two-dimensional problem. This is due to the fact that this diagonal is at a 45° angle from our grid lines. Here, we take $\beta = 1.2$, and the corresponding smooth steady-state solution of this problem is $u(x,y) = \sin\left(\frac{x+y}{\sqrt{2}}\right)$. The corresponding errors and convergence orders of the MR-HWENO5, MR-WENO5 and WENO5-Z schemes are listed in Table 3.3. Similar to the results in Table 3.1, the L^1 error can still reach fifth-order precision, while the L^∞ error is only fourth-order precision. The error of the MR-HWENO5 scheme is smaller than that of the other two schemes for the same mesh size. The convergence history of the average residual varying with

the number of iterations is shown in Figure 3.9. As shown in the figure, the residuals corresponding to all schemes can be reduced to machine accuracy, and the residual of MR-HWENO5 scheme reduces faster than that of the other two schemes.

Table 3.3: 2D-Burgers' equation: $s(x,y) = \sin\left(\frac{x+y}{\sqrt{2}}\right)\cos\left(\frac{x+y}{\sqrt{2}}\right), \beta = 1.2$. The initial condition $u(x,y,0) = 1.2\sin\left(\frac{x+y}{\sqrt{2}}\right)$. The exact boundary condition. L^1 and L^∞ error.

	MR-HWENO5 scheme				MR-WENO5 scheme			
grid points	L^1 error	order	L^∞ error	order	L^1 error	order	L^∞ error	order
20×20	3.86E-07		5.88E-06		2.20E-08		3.16E-07	
30×30	1.18E-09	17.2	1.51E-08	17.7	4.06E-09	5.02	8.03E-08	4.07
40×40	1.43E-10	8.39	3.72E-09	5.57	1.15E-09	5.01	2.90E-08	4.05
50×50	5.20E-11	5.04	1.68E-09	3.96	4.22E-10	5.01	1.26E-08	4.14
60×60	2.32E-11	4.83	8.67E-10	3.96	1.83E-10	5.01	6.25E-09	4.21
70×70	1.19E-11	4.70	4.96E-10	3.90	8.92E-11	5.00	3.40E-09	4.26

	WENO5-Z scheme			
grid points	L^1 error	order	L^∞ error	order
20×20	2.20E-08		3.16E-07	
30×30	4.06E-09	5.02	8.03E-08	4.07
40×40	1.15E-09	5.01	2.90E-08	4.05
50×50	4.21E-10	5.01	1.26E-08	4.14
60×60	1.83E-10	5.01	6.25E-09	4.21
70×70	8.92E-11	5.00	3.40E-09	4.26

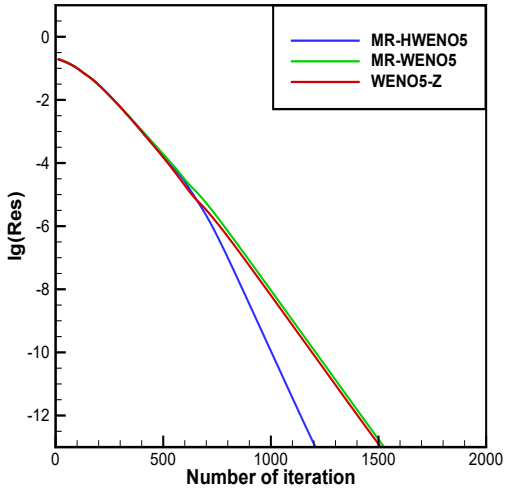

Figure 3.9: 2D-Burgers' equation: $s(x,y) = \sin\left(\frac{x+y}{\sqrt{2}}\right)\cos\left(\frac{x+y}{\sqrt{2}}\right), \beta = 1.2$. The convergence history of the average residual. Number of cells: 70×70.

Example 3.6. The two-dimensional Euler equations:

$$\begin{pmatrix} \rho u \\ \rho u^2 + p \\ \rho uv \\ u(E+p) \end{pmatrix}_x + \begin{pmatrix} \rho v \\ \rho uv \\ \rho v^2 + p \\ v(E+p) \end{pmatrix}_y = 0, \quad (x, y) \in [0, 2\pi] \times [0, 2\pi], \tag{3.11}$$

here ρ is the density, (u, v) is the velocity, E is the total energy, γ is the gas constant which is again taken as 1.4 and $p = (\gamma - 1)(E - \frac{1}{2}(\rho u^2 + \rho v^2))$ is the pressure. For this problem, there are many possible steady-state solutions, for example:

(1) $\rho(x, y, \infty) = 1 + 0.2(x - y)$, $u(x, y, \infty) = 1$, $v(x, y, \infty) = 1$, $p(x, y, \infty) = 1$;

(2) $\rho(x, y, \infty) = 1 + 0.2(2(x - y))$, $u(x, y, \infty) = 1$, $v(x, y, \infty) = 1$, $p(x, y, \infty) = 1$.

We take the initial conditions and boundary conditions in both directions to be the two exact steady-state solutions above, respectively. The corresponding errors and convergence orders of the MR-HWENO5, MR-WENO5 and WENO5-Z schemes are listed in Table 3.4, where the expected fifth-order accuracy in the L^1 norm and the L^∞ norm is observed. The error of MR-HWENO5 scheme is still much smaller than that of the other two schemes under the same mesh size. The convergence history of the average residual varying with the number of iterations is shown in Figure 3.10. As shown in the figure, although all these schemes can converge to machine accuracy, the residual of the MR-HWENO5 scheme is smaller than that of the other two schemes in the initial stage and achieves machine accuracy in fewer steps.

Example 3.7. The two-dimensional Euler equations (3.11) in region $[0, 4] \times [0, 1]$. The initial condition is

$$(\rho, u, v, p) = \left(1, 2.9, 0, \frac{1}{\gamma}\right). \tag{3.12}$$

As for the boundary condition, it is taken to be $(\rho, u, v, p) = (1.69997, 2.61934, -0.50632, 1.52819)$ on the upper boundary $y = 1$ and it is a reflective boundary on the lower boundary $y = 0$. The left boundary at $x = 0$ is an inflow with $(\rho, u, v, p) = \left(1, 2.9, 0, \frac{1}{\gamma}\right)$, and the right boundary at $x = 4$ is an outflow. This problem was considered as a regular shock reflection problem of the two-dimensional Euler equations in [5]. The contours and the cross-sections at $y = 0.1$ and $y = 0.5$ of the numerical results by the MR-HWENO5, MR-WENO5 and WENO5-Z schemes are displayed in Figure 3.11. Figure 3.12 displays the convergence history of the average residual varying with the number of iterations. It is observed that the declining trend

Table 3.4: 2D-Euler equations. The exact initial condition. The exact boundary condition. L^1 and L^∞ error.

	case (1)							
	MR-HWENO5 scheme				MR-WENO5 scheme			
grid points	L^1 error	order	L^∞ error	order	L^1 error	order	L^∞ error	order
20×20	9.00E-06		4.12E-05		5.16E-05		2.22E-04	
30×30	1.28E-06	5.01	5.87E-06	5.00	7.39E-06	4.99	3.25E-05	4.93
40×40	3.16E-07	5.00	1.47E-06	4.96	1.82E-06	5.01	8.14E-06	4.95
50×50	1.06E-07	5.00	4.95E-07	4.97	6.10E-07	5.01	2.74E-06	4.98
60×60	4.34E-08	5.00	2.03E-07	4.99	2.49E-07	5.01	1.12E-06	4.98
70×70	2.03E-08	5.00	9.50E-08	4.99	1.16E-07	5.01	5.27E-07	5.00
	case (1)				case (2)			
	WENO5-Z scheme				MR-HWENO5 scheme			
grid points	L^1 error	order	L^∞ error	order	L^1 error	order	L^∞ error	order
20×20	5.47E-05		2.40E-04		6.08E-04		2.89E-03	
30×30	7.46E-06	5.12	3.45E-05	4.98	8.34E-05	5.10	4.57E-04	4.73
40×40	1.82E-06	5.03	8.39E-06	5.06	2.02E-05	5.08	1.08E-04	5.15
50×50	6.10E-07	5.02	2.81E-06	5.02	6.74E-06	5.03	3.65E-05	4.99
60×60	2.49E-07	5.02	1.14E-06	5.02	2.73E-06	5.03	1.48E-05	5.02
70×70	1.16E-07	5.01	5.34E-07	5.01	1.28E-06	5.01	6.88E-06	5.06
	case (2)							
	MR-WENO5 scheme				WENO5-Z scheme			
grid points	L^1 error	order	L^∞ error	order	L^1 error	order	L^∞ error	order
20×20	3.10E-03		1.46E-02		3.67E-03		1.56E-02	
30×30	4.61E-04	4.90	2.16E-03	4.90	5.25E-04	4.99	2.42E-03	4.78
40×40	1.16E-04	4.95	5.69E-04	4.77	1.24E-04	5.15	6.14E-04	4.90
50×50	3.91E-05	4.96	1.99E-04	4.82	4.05E-05	5.14	2.10E-04	4.93
60×60	1.61E-05	4.97	8.20E-05	4.95	1.63E-05	5.08	8.56E-05	5.00
70×70	7.53E-06	4.99	3.83E-05	5.02	7.58E-06	5.04	3.98E-05	5.04

of residual is almost the same for both the MR-HWENO5 scheme and the MR-WENO5 scheme, and the residuals when they reach the steady state are much smaller than that of the WENO5-Z scheme.

Example 3.8. A supersonic flow past a plate with an attack angle $\alpha = 10^\circ$ problem:

(1) the calculation region is chosen to be $[0, 10] \times [-5, 5]$ with a plate located at $x \in [1, 2], y = 0$;

(2) the calculation region is chosen to be $[0, 7] \times [-5, 5]$ with a plate located at $x \in [2, 7], y = 0$.

The governing equation is the two-dimensional Euler equations (3.11). The initial condition is $(p, \rho, \mu, \nu) = (\frac{1}{\gamma(Ma_\infty)^2}, 1, \cos(\alpha), \sin(\alpha))$, where the free stream Mach number is $Ma_\infty = 3$. The physical values of the inflow and outflow boundary conditions are applied in each direction, and the slip boundary condition is imposed on the plate. The contours of the numerical results by the MR-HWENO5, MR-WENO5 and WENO5-Z schemes are displayed in Figure 3.13. Figure 3.14 displays the convergence history of the average

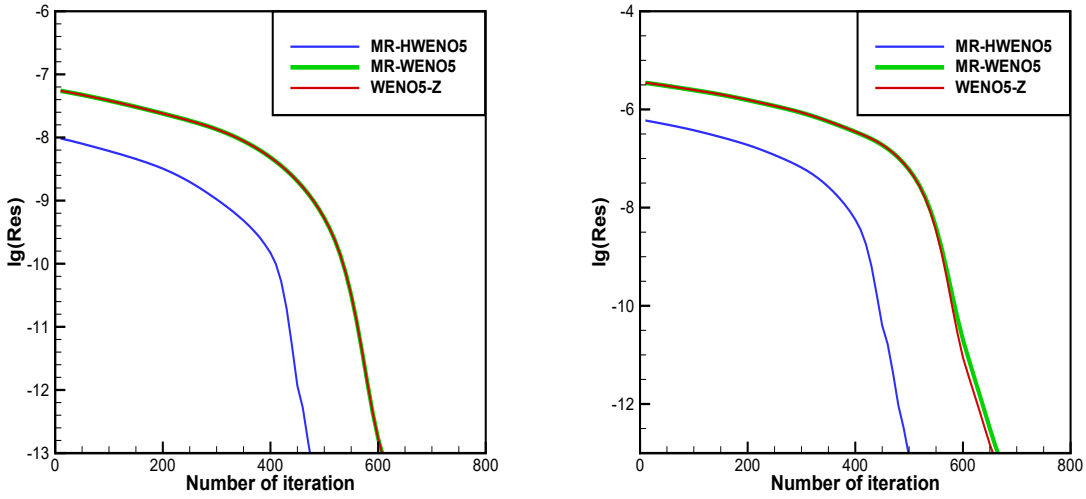

Figure 3.10: 2D-Euler equations. Left: case(1); right: case(2). The convergence history of the average residual. Number of cells: 70×70.

residual varying with the number of iterations. We can observe that apart from the WENO5-Z scheme, the residuals of the other two schemes can be reduced to machine accuracy, and the residual of MR-HWENO5 scheme decreases faster than that of MR-WENO5 scheme for both cases. Furthermore, from Figure 3.15, which shows the results of case(1) and case(2) with $\epsilon = 10^{-6}, 10^{-10}, 10^{-12}, 10^{-40}$ in (2.16), we can come to a conclusion that the ϵ does affect the convergence of the average residual. In general, the smaller the ϵ, the worse the convergence. This is also why we change $\epsilon = 10^{-10}$ in [22, 23] to $\epsilon = 10^{-6}$ in (2.16), which is consistent with the parameter setting in reference [47].

4 Concluding remarks

In this paper, we apply the derivative-based finite-volume MR-HWENO scheme in [22] to solve the steady-state problems. The scheme in this paper possesses the same reconstruction and updating process for the function value as in [22], but differs for the derivative value. Instead of evolving in time, the derivative value at the next time step is obtained by a direct linear interpolation of the derivative value at the current time step together with the function value at the next time step in the sense of cell average. Since the problems we are dealing with are steady, such a misalignment in time does not have much effect on the accuracy in the smooth region and the resolution near the discontinuity of the scheme. The main advantage

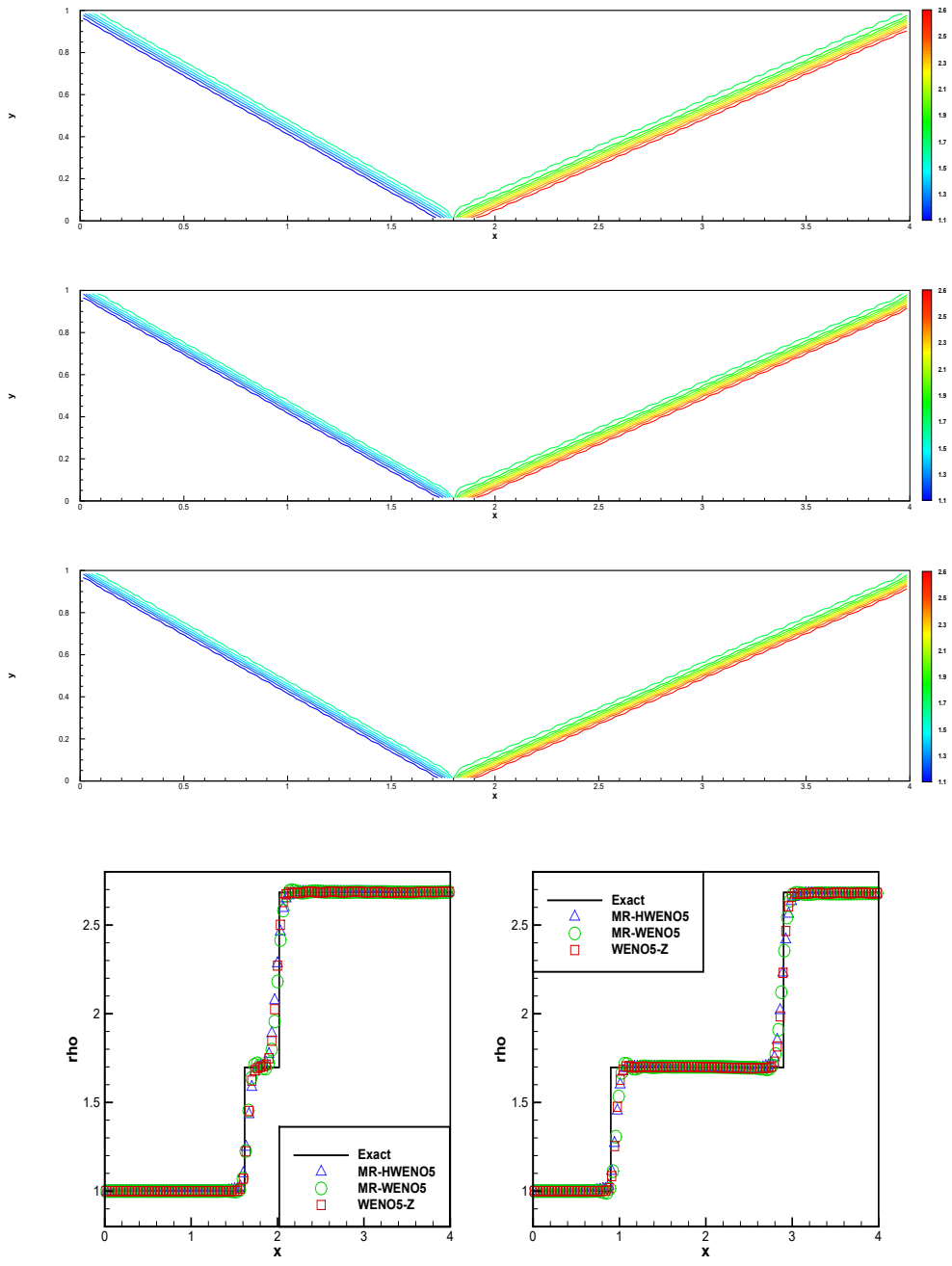

Figure 3.11: Regular shock reflection problem of the 2D-Euler equations. Top: 15 equally spaced contours for ρ of the numerical results by the MR-HWENO5, MR-WENO5 and WENO5-Z schemes from 1.10 to 2.58; bottom: the cross-sections at $y = 0.1$ and $y = 0.5$. Number of cells: 120×30.

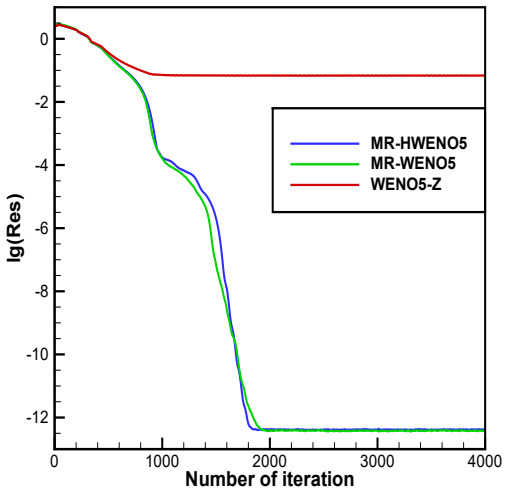

Figure 3.12: Regular shock reflection problem of the 2D-Euler equations. The convergence history of the average residual. Number of cells: 120×30.

of the MR-HWENO scheme for steady-state problems is that it simplifies the calculation of the derivative. Moreover, the CFL number can still be chosen to be 0.6 in both one- and two-dimensional cases, while the CFL number is only 0.3 for the residual distribution WENO scheme in [26] and 0.2 for the residual distribution HWENO scheme in two-dimensional case in [27]. The numerical results in the previous section further show that the residual of MR-HWENO scheme can converge to machine accuracy or an extremely small number, and falls either faster than or just as fast as the MR-WENO and WENO-Z schemes.

This paper pays more attention to whether the scheme can converge to the solution of the problem quickly and correctly. Its numerical performance in certain problems (e.g. one-dimensional nozzle flow problem Example 3.4) still needs to be further improved, in terms of better capturing of discontinuity and better suppression of oscillations, which also provides a direction for our future research.

For the sake of simplicity, this paper mainly considers the MR-HWENO scheme on uniform meshes, except for some numerical experiments in Examples 3.1 and 3.4. We will consider more non-uniform and unstructured meshes in our future research.

Figure 3.15 shows that the ϵ in (2.16) does affect the convergence of the average residual. In general, the smaller the ϵ, the worse the convergence. Thus, it is worth studying a method that is not sensitive to ϵ in terms of good convergence for the steady-state problems.

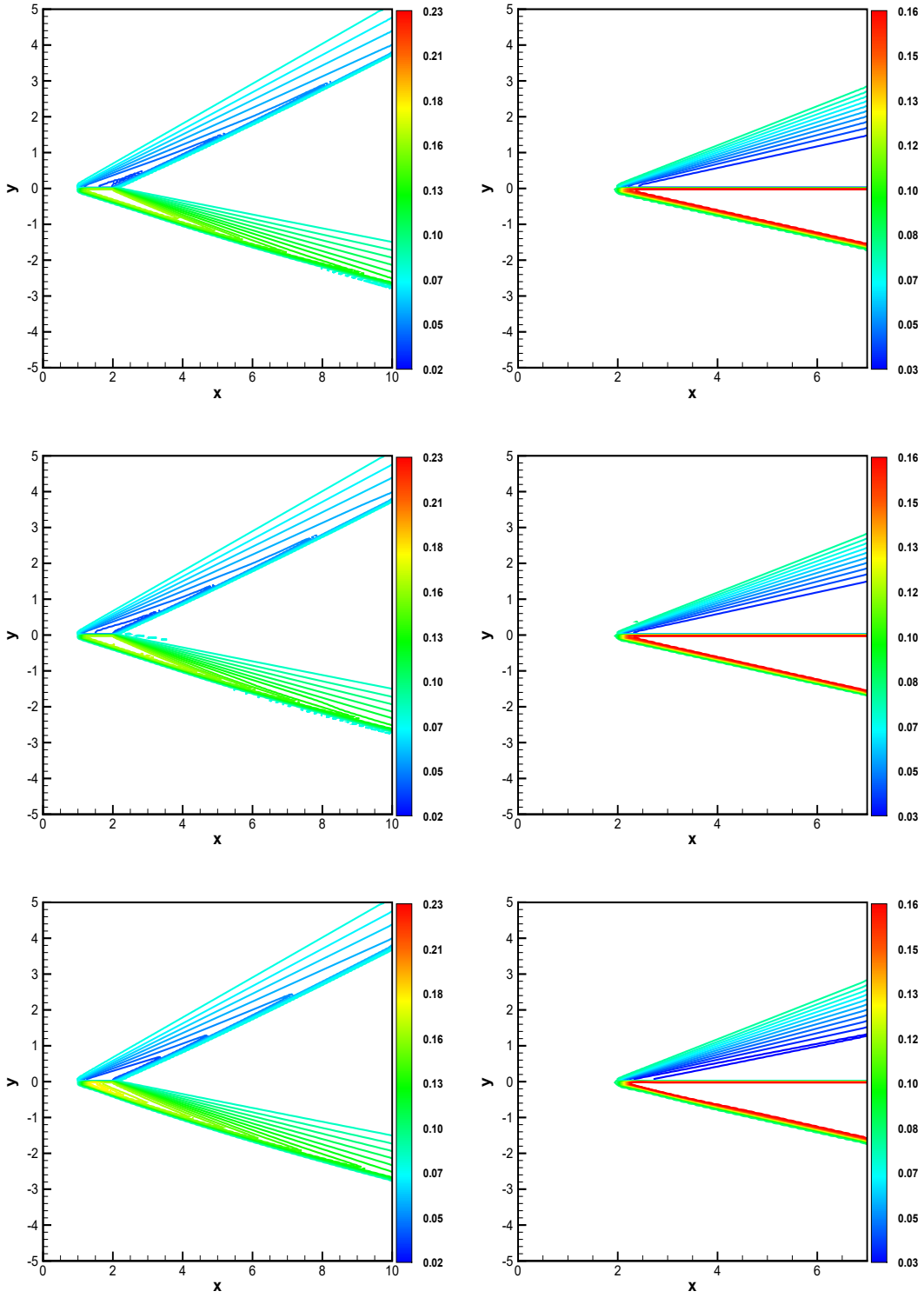

Figure 3.13: A supersonic flow past a plate with an attack angle problem. Left: 30 equally spaced contours for pressure p of the numerical results for case(1) by the MR-HWENO5, MR-WENO5 and WENO5-Z schemes from 0.02 to 0.23 . Number of cells: 200×200. Right: 30 equally spaced contours for pressure p of the numerical results for case(2) by the MR-HWENO5, MR-WENO5 and WENO5-Z schemes from 0.031 to 0.161. Number of cells: 140×200.

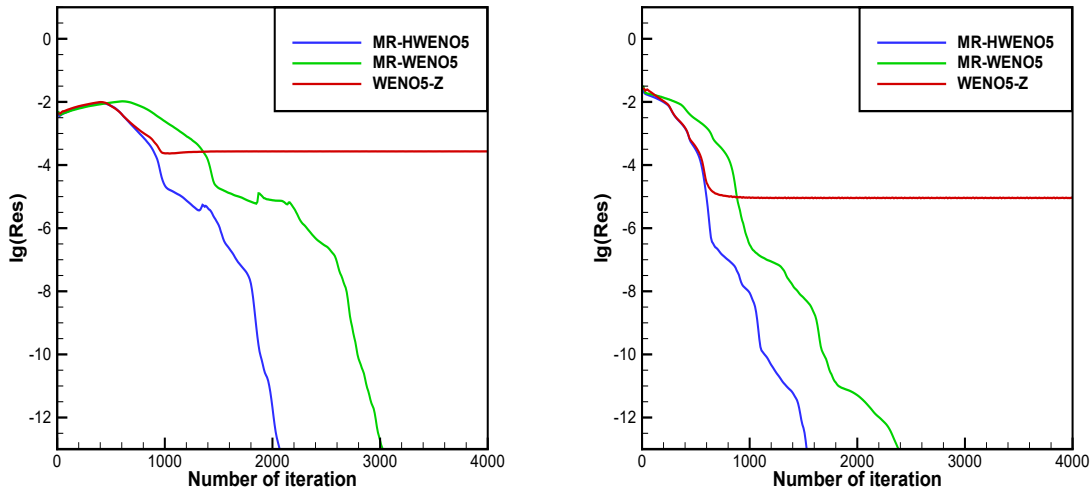

Figure 3.14: A supersonic flow past a plate with an attack angle problem. The convergence history of the average residual. Left: case(1). Number of cells: 200×200. Right: case(2). Number of cells: 140×200.

Acknowledgement. We would like to thank Professor Jun Zhu in Nanjing University of Aeronautics and Astronautics for providing coding support for some examples.

References

[1] R. Abgrall, Multiresolution analysis on unstructured meshes: application to CFD, Clarendon, Oxford, (1995).

[2] R. Abgrall, Multiresolution analysis on unstructured meshes: application to CFD, Computational Methods in Applied Sciences, 2(1997), 147-156.

[3] R. Abgrall, A. Harten, Multiresolution representation in unstructured meshes, SIAM J. Numer. Anal., 35(1998), 2128-2146.

[4] R. Bürger, A. Kozakevicius, Adaptive multiresolution WENO schemes for multi-species kinematic flow models, J. Comput. Phys., 224(2007), 1190-1222.

[5] W. Cai, D. Gottlieb, and C.-W. Shu, Essentially non-oscillatory spectral Fourier methods for shock wave calculations, Math. Comp., 52(1989), 389-410.

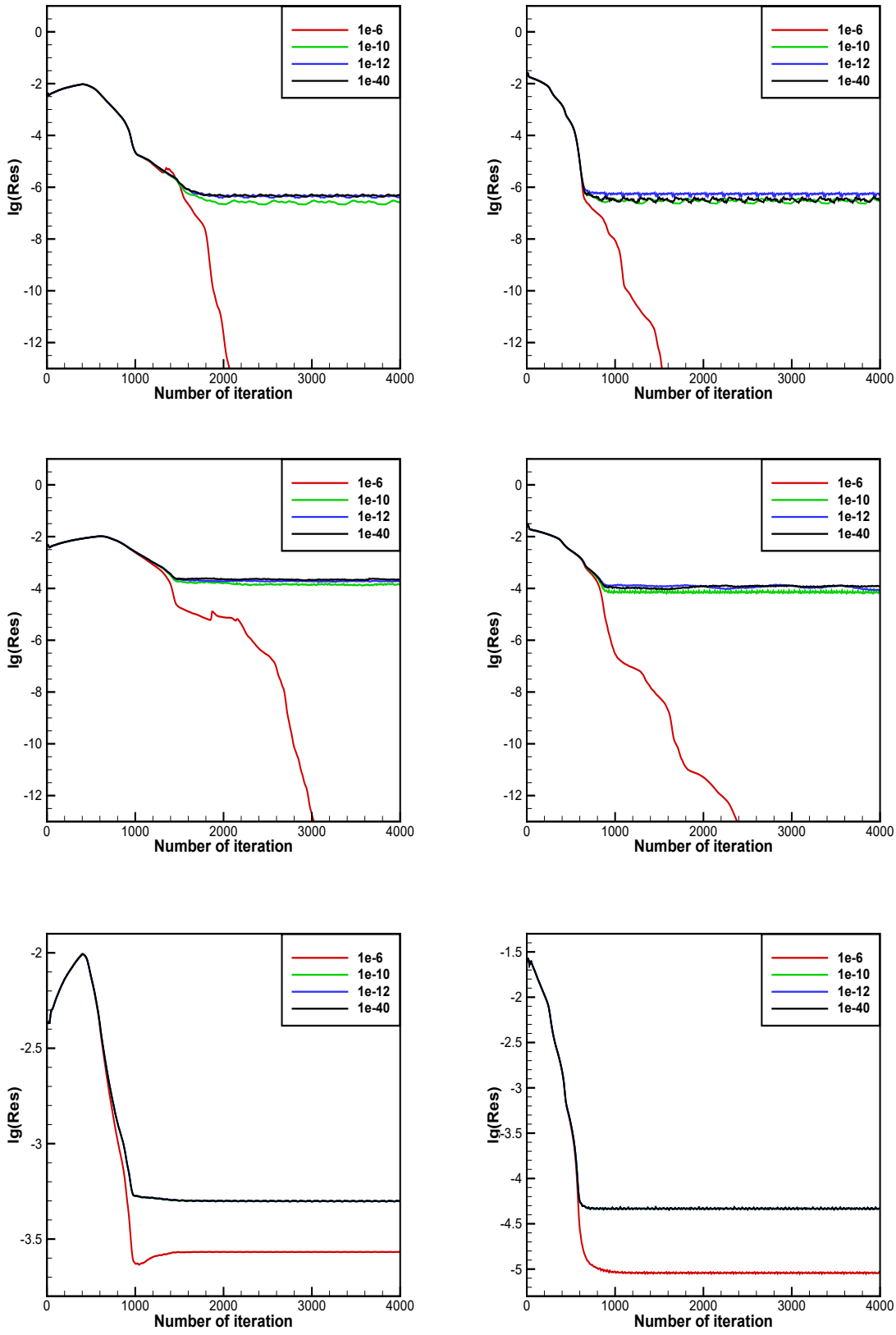

Figure 3.15: A supersonic flow past a plate with an attack angle problem. The convergence history of the average residual. Left: case(1). Number of cells: 200×200. Right: case(2). Number of cells: 140×200. From top to bottom: MR-HWENO5, MR-WENO5, WENO5-Z.

[6] S. Chen, Fixed-point fast sweeping WENO methods for steady state solution of scalar hyperbolic conservation laws, Int. J. Numer. Anal. Mod., 11(2014), 117-130.

[7] G. Chiavassa, R. Donat, S. Muller, Multiresolution-based adaptive schemes for hyperbolic conservation laws, Lecture Notes in Computational Science and Engineering, 41(2003), 137-159.

[8] S.S. Chu, A. Kurganov, S. Mohammadian, Z.D. Zheng, Fifth-order A-WENO path-conservative central-upwind scheme for behavioral non-equilibrium traffic models, Commun. Comput. Phys., 33(2023), 692-732.

[9] W. Dahmen, B. Gottschlich-Muller, S. Muller, Multiresolution schemes for conservation laws, Numer. Math., 88(2001), 399-443.

[10] P. Embid, J. Goodman, A. Majda, Multiple steady states for 1-D transonic flow, SIAM J. Sci. Statist. Comput., 5(1984), 21-41.

[11] S. Gottlieb, C.-W. Shu, E. Tadmor, Strong stability preserving high order time discretization Methods, SIAM Rev., 43(2001), 89-112.

[12] W. Hao, J.D. Hauenstein, C.-W. Shu, A.J. Sommese, Z. Xu, Y.-T. Zhang, A homotopy method based on WENO schemes for solving steady state problems of hyperbolic conservation laws, J. Comput. Phys., 250(2013), 332-346.

[13] A. Harten, High resolution schemes for hyperbolic conservation laws, J. Comput. Phys., 49(1983), 357-393.

[14] A. Harten, Multi-resolution analysis for ENO schemes, Institute for Computer Applications in Science and Engineering, NASA Langley Research Center, Hampton, Virginia, 23665-5225, Contract No. NAS1-18605(1991).

[15] A. Harten, Discrete multi-resolution analysis and generalized wavelets. Appl. Numer. Math., 12(1993), 153-192.

[16] A. Harten, Adaptive multiresolution schemes for shock computations, J. Comput. Phys., 115(1994), 319-338.

[17] A. Harten, Multiresolution algorithms for the numerical solution of hyperbolic conservation laws, Commun. Pure Appl. Math., 48(1995), 1305-1342.

[18] A. Harten, Multiresolution representation of data: a general framework, SIAM J. Numer. Anal., 33(1996), 1205-1256.

[19] A. Harten, B. Engquist, S. Osher, S. Chakravarthy, Uniformly high order accurate essentially non-oscillatory schemes, III, J. Comput. Phys., 71(1987), 231-303.

[20] C. Hu, C.-W. Shu, Weighted essentially non-oscillatory schemes on triangular meshes, J. Comput. Phys., 150(1999), 97-127.

[21] G.-S. Jiang, C.-W. Shu, Efficient implementation of weighted ENO schemes, J. Comput. Phys., 126(1996), 202-228.

[22] J. Li, C.-W. Shu, J. Qiu, Multi-resolution HWENO schemes for hyperbolic conservation laws, J. Comput. Phys., 446(2021), 110653.

[23] J. Li, C.-W. Shu, J. Qiu, Moment-based multi-resolution HWENO scheme for hyperbolic conservation laws, Commun. Comput. Phys., 32(2022), 364-400.

[24] L. Li, J. Zhu, C.-W. Shu, Y.-T. Zhang, A fixed-point fast sweeping WENO method with inverse lax-wendroff boundary treatment for steady state of hyperbolic conservation laws, Commun. Appl. Math. Comp., 5(2023), 403-427.

[25] L. Li, J. Zhu, Y.-T. Zhang, Absolutely Convergent fixed-point fast sweeping WENO methods for steady state of hyperbolic conservation laws, J. Comput. Phys., 443(2021), 110516.

[26] J. Lin, R. Abgrall, J. Qiu, High order residual distribution for steady state problems for hyperbolic conservation laws, J. Sci. Comput., 79(2019), 891-913.

[27] J. Lin, Y. Ren, R. Abgrall, J. Qiu, High order residual distribution conservative finite difference HWENO scheme for steady state problems, J. Comput. Phys., 457(2022), 111045.

[28] X.D. Liu, S. Osher, T. Chan, Weighted essentially non-oscillatory schemes, J. Comput. Phys., 115(1994), 200-212.

[29] Y.Z. Lu, J. Zhu, S.Z. Cui, Z.M. Wang, L.L. Tian, N. Zhao, High-order local discontinuous Galerkin method with multi-resolution WENO limiter for Navier-Stokes equations on triangular meshes, Commun. Comput. Phys., 33(2023), 1217-1239.

[30] J. Qiu, C.-W. Shu, Hermite WENO schemes and their application as limiters for Runge-Kutta discontinuous Galerkin method: one-dimensional case, J. Comput. Phys., 193(2004), 115-135.

[31] J. Qiu, C.-W. Shu, Hermite WENO schemes and their application as limiters for Runge-Kutta discontinuous Galerkin method II: Two-dimensional case, Comput. Fluids, 34(2005), 642-663.

[32] M.D. Salas, S. Abarbanel, and D. Gottlieb, Multiple steady states for characteristic initial value problems, Appl. Numer. Math., 2(1986), 193-210.

[33] S. Serna, A. Marquina, Power ENO methods: a fifth-order accurate weighted power ENO method, J. Comput. Phys., 194(2004), 632-658.

[34] J. Shi, Y.-T. Zhang, C.-W. Shu, Resolution of high-order WENO schemes for complicated flow structures, J. Comput. Phys., 186(2003), 690-696.

[35] C.-W. Shu, S. Osher, Efficient implementation of essentially non-oscillatory shock capturing schemes, J. Comput. Phys., 77(1988), 439-471.

[36] C.-W. Shu, S. Osher, Efficient implementation of essentially non-oscillatory shock capturing schemes, II, J. Comput. Phys., 83(1989), 32-78.

[37] Y.F. Wan, Y.H. Xia, A hybrid WENO scheme for steady-state simulations of Euler equations, J. Comput. Phys., 463(2022), 111292.

[38] Y.F. Wan, Y.H. Xia, A hybrid WENO scheme for steady Euler equations in curved geometries on Cartesian grids, Commun. Comput. Phys., 33(2023), 1270-1331.

[39] L. Wu, Y.-T. Zhang, S. Zhang, C.-W. Shu, High order fixed-point sweeping WENO methods for steady state of hyperbolic conservation laws and its convergence study, Commun. Comput. Phys., 20(2016), 835-869.

[40] Y.H. Zahran, A.H. Abdalla, Seventh order Hermite WENO scheme for hyperbolic conservation laws, Comput. Fluids, 131(2016), 66-80.

[41] S. Zhang, S. Jiang, C.-W. Shu, Improvement of convergence to steady state solutions of Euler equations with the WENO schemes, J. Sci. Comput., 47(2011), 216-238.

[42] S. Zhang, C.-W. Shu, A new smoothness indicator for the WENO schemes and its effect on the convergence to steady state solutions, J. Sci. Comput., 31(2007), 273-305.

[43] Z. Zhao, Y. Chen, J. Qiu, A hybrid Hermite WENO scheme for hyperbolic conservation laws, J. Comput. Phys., 405(2020), 109175.

[44] Z. Zhao, J. Qiu, A Hermite WENO scheme with artificial linear weights for hyperbolic conservation laws, J. Comput. Phys., 417(2020), 109583.

[45] J. Zhu, J. Qiu, A class of forth order finite volume Hermite weighted essentially non-oscillatory Schemes, Science in China, Series A–Mathematics, 51(2008), 1549-1560.

[46] J. Zhu, C.-W. Shu, A new type of multi-resolution WENO schemes with increasingly higher order of accuracy, J. Comput. Phys., 375(2018), 659-683.

[47] J. Zhu, C.-W. Shu, Convergence to steady-state solutions of the new type of high-order multi-resolution WENO schemes: a numerical study, Commun. Appl. Math. Comput., 2(2019), 429-460.

[48] J. Zhu, C.-W. Shu, A new type of multi-resolution WENO schemes with increasingly higher order of accuracy on triangular meshes, J. Comput. Phys., 392(2019), 19-33.